Supplementary Information for 'Two-phase orogen-wide extension of the Himalaya since Miocene'

Rabindra Kumar Patel[1,2], Vikas Adlakha[1,2*], Kunal Mukherjee[1], Shailendra Pundir[1], Parikshita Pradhan[1,2], Ramesh Chandra Patel[3]

[1]Wadia Institute of Himalayan Geology, Dehradun, India

[2]Academy of Scientific and Innovative Research, India

[3]Department of Geology, Institute of Science, Banaras Hindu University, Varanasi, India

e-mail: vikas.himg@gmail.com

Contents

2.3.7 Kangmar Dome

3. Normalized Channel Steepness Index (Ksn)

4. Gravity Disturbance

1. Swath Profiles

To analyze the relationship between topography, precipitation with faults in gneissic domes (See Fig. 1), we plotted swath profiles spanning over ~400 km, extending from the Main Himalayan Thrust (MHT) to the Indus Tsangpo Suture Zone (ITSZ) (see Fig. S1). In this study, swath profiles are extracted from SRTM 30m DEM using ArcGIS add-on software (Periz-Pena et al., 2017), with a swath width of ~50 km (see Fig. 1). The correlation between elevation, relief, and precipitation, incorporating Tropical Rainfall Measuring Mission (TRMM) annual rainfall data (1998–2009) (see Figure S1) (Bookhagen, 2010), clearly demonstrates that all the gneissic domes are situated in the rain shadow area of the Himalaya.

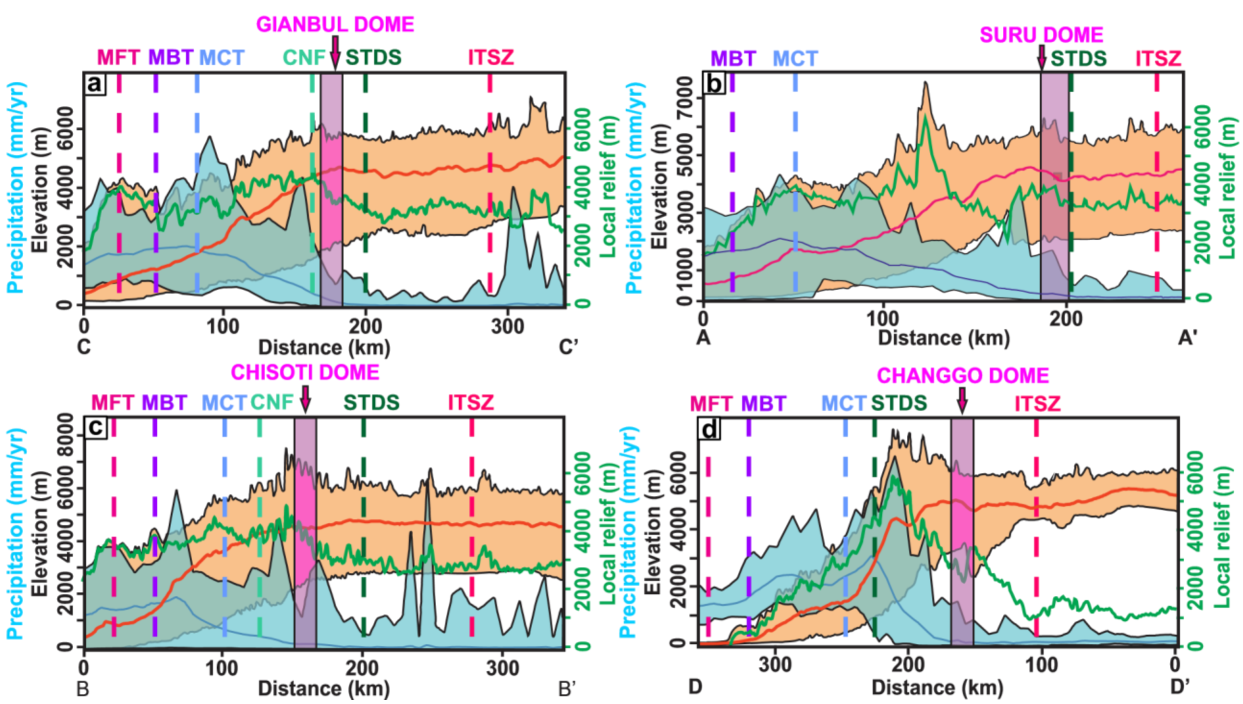

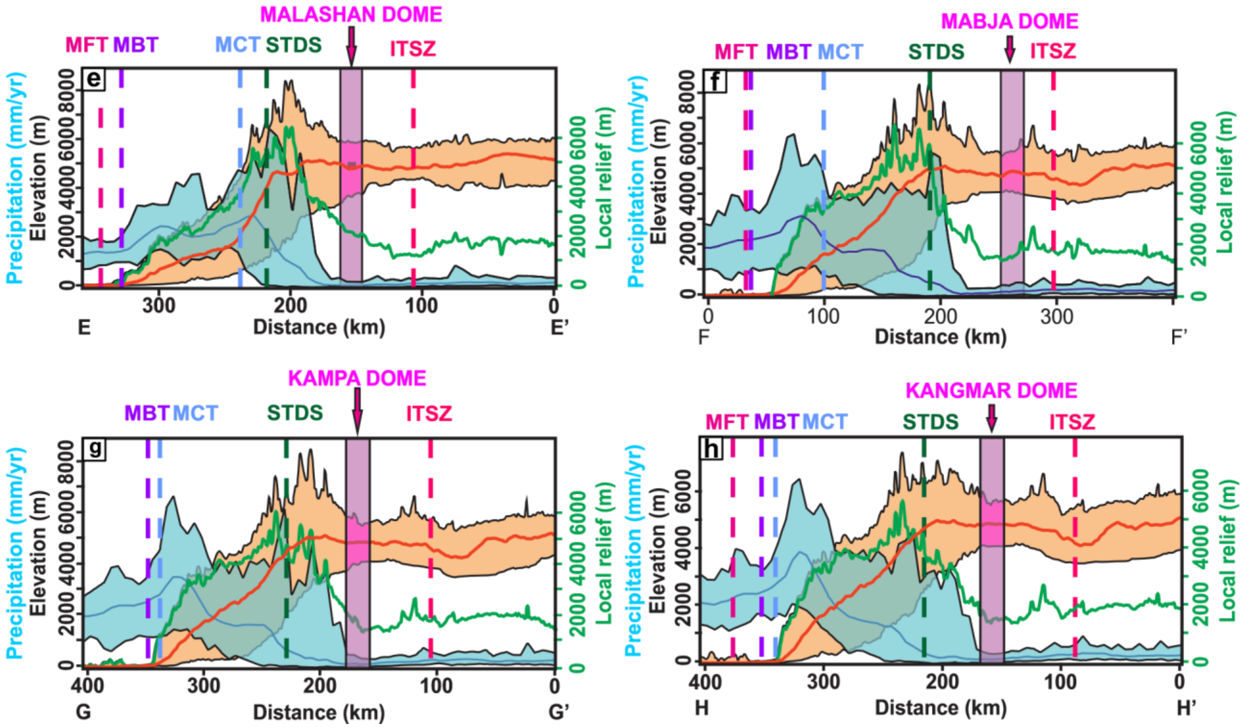

Fig. S1: Figures a-h illustrate the swath profiles for the gneissic domes in the Himalaya, having swath lines illustrated in Fig. 1.

2. Thermo-kinematic Modeling

Pecube is a finite element code (Braun, 2003) used for thermo-kinematic modeling, which solves the heat transport equation for the lithospheric plate/crust and helps understand the cooling age pattern in the orogenic belt. Kinematic modeling helps with the rock transport process using fault geometries, and the thermal model helps to calculate fault motion, surface erosion, and thermal properties (Braun, 2012). The Pecube tool is used for those tectonic crusts affected by the exhumation, denudation, and Surface uplift processes. In this modeling, we used different parameters and the thermochronological ages mentioned in Supplementary Table S1a-b and Table S3. In the output VTK file, we visualize the isotherm profile in the 3D model, and those 3D models are shown in Supplementary Fig. S2, S8, S11, S14, S17, S20, and S23. Pecube is a Fortran90 code

Program compiled by using the GCC compiler, and all the installation processes are mentioned in the user guide provided by Jean Braun's GitHub page (*GitHub - jeanbraun/Pecube: Thermo-kinematic model to invert thermochronological data*). Broun mentioned all the fundamental equations (Braun, 2003; Braun et al., 2012), it is a great tool for geological research (Coutand et al., 2014). Finally, Pecube gives the synthetic cooling ages and exact activation time using the observed cooling ages and different fault geometries for thermo-kinematic modeling. In this case, we performed both forward and inverse models to determine the timing of activation of those gneissic domes (See Fig. 1).

The heat transportation equation is:

$$pc\left(\frac{\partial T}{\partial t} + v\frac{\partial T}{\partial z}\right) = \frac{\partial}{\partial x}k\frac{\partial T}{\partial x} + \frac{\partial}{\partial y}k\frac{\partial T}{\partial y} + \frac{\partial T}{\partial z}k\frac{\partial T}{\partial z} + pA$$

Where x,y, and z are the coordinates in the three directions,

t = time (Ma),

T = Temperature (°C),

p = Density of the rock (kg /m^3)

c = Heat capacity (J kg^{-1} K^{-1})

v = Vertical Velocity of the rock (km Ma^{-1})

k = conductivity (W m^{-1} k $^{-1}$)

A = Radiogenic heat production (μW m^{-3})

k, ck, and p remain constant through time.

This heat-transport equation solves and reflects denudation, and surface changes the rock particle transport in both the vertical and lateral directions, reflected in the 3D model.

2.1 Forward Modeling

We performed a 3D forward model using Pecube (Braun, 2003; Braun et al., 2012), representing the geothermal gradient profile by solving the heat-transport equation. For the 3D models, we used present-day surface topography as a dat file extracted from SRTM 30m DEM (Open Topography), where we used different parameters, such as heat production, thermal diffusivity, basal temperature, fault advection, etc., to predict cooling ages for different gneissic domes in the Himalaya (Adlakha et al., 2013).

In this modeling, fault motion was the dip-slip along the fault model, and all those fault parameters were taken from different research papers given in the supplementary discussion section 2.3.1-2.3.7, whereas shear heating and isostasy are not considered for the evolution of this gneissic dome due to its minimal effect (Herman et al., 2010), while fault advection parameter are considered. Here, in the forward model, we performed two times kinematics tectonic scenarios using the Muscovite Argon (MAr), Biotite Argon (BAr), Zircon Fission Track (ZFT), Zircon Helium (ZHe), and Apatite Fission Track (AFT) ages (Supplementary Table S1a-b) for the forward and inverse modeling. Finally, the root mean square (RMS) misfit between observed and predicted ages is expressed over a million years (See modeling discussion).

In this study, we have used only the flat ramp model, where we have utilized different in-depth data and earthquake data from various research papers, and the details of the fault data are discussed in the modeling discussion section. For the 3D model, we have considered the MHT, MCT, STDS, and local-scale faults taken from different research papers given in the model discussion section, where the convergence rate has been kept constant at ~17-24 km/Myr, partitioned into underthrusting and overthrusting segments (Decelles et al., 2004; Avouac, 2003; Herman et al., 2010).

2.2 Inverse Modeling

Inverse modeling is done using the Neighborhood Algorithm (Sambridge, 1999b, 1999a), which runs several forward models to determine the best-fit outcome, where each dot represents a forward model. To employ the inverse model, we need to set the parameters for forward modeling, whereas, for the inverse model, we can set the range of different parameters for the inverse model to find the best fit. The inverse model's result is displayed in Supplementary Figs. S4, S10, S13, S16, S19, S22, and S25.

The misfit was calculated using the formula:

$$M = \sqrt{\frac{1}{N}\sum_{i=1}^{N}\frac{(O_i - P_i)^2}{\sigma_i^2}}$$

Where N = Number of data points for the thermochronometer.

O_i = Observed ages,

P_i = Predicted ages,

σ_i= 1σ uncertainty in observed ages.

The neighborhood algorithm's importance is that it searches for the best fit among multiple parameters and minimizes the misfit between predicted and observed data (Sambridge, 1999a).

2.3 Modeling Discussion

2.3.1 Gianbul Dome

The Gianbul dome was modeled using the fault geometry from Hazarika et al. (2017), exhibiting a two-stage tectonic scenario from 26 million years ago to the present day. To simulate the model, we used four fault data employed for the 3D modeling, with two faults (MHT and MCT) modeled as thrust fault geometry, while the other two faults (CNF and STDS) were modeled as normal fault geometry. Whereas the CNF fault data was obtained from (Yadav et al., 2016), and

MCT structure was obtained using inverse modeling, with the ranges given in Supplementary Table S4. For the Forward model, the thickness was set to 40 km, and all the parameters used for the modeling are listed in Supplementary Table S3. To run this model, we employed five types of thermochronological data (MAr, BAr, ZFT, ZHe, and AFT) (See Table S1a-b), age elevation relation parameter, and fault advection parameter were incorporated, while the fission track predicted data model was based on the Richard Ketcham routine. The period of activity of MHT was considered from 26 million years ago to the present day, while in the case of MCT, only a one-time scenario was taken between 21-20 Ma, as no significant effect on the predicted age model was observed if we activated it for other times, especially considered for the Gianbul Dome. In contrast, for STDS, two time scenarios were taken between 21 to 20 Ma and 6.5 to 6 Ma, whereas in both the tectonic scenarios, STDS was considered a normal fault geometry to satisfy all the synthetic ages with the observed ones. The same approach was modeled for CNF, which was considered for two-time scenarios between 21-20 Ma and 6.5 to 6 Ma. As a result, the best RMS misfit is 2.36 Ma for the forward model, and all the forward and inverse model figures are attached in the supplementary Fig. S2-S4 and have ranges for the inverse model and misfit, as given in Supplementary Table S4.

The table below shows the number of model scenario tests to constrain the best RMS misfit.

Dome Names	Faults	Fault Parameters Used	RMS Misfit (Ma)	RMS Total Misfit (Ma)
Gianbul Dome (AFT, ZFT, MAR, BAR)	Model Scenario 1 (Except MCT 2nd activation)	MHT (26 Ma-0 Ma) MCT (21 Ma-20Ma) CNF (21Ma-20 Ma, 6.5 Ma-6.0 Ma) STDS (21Ma-20 Ma, 6.5 Ma-6.0	AFT = 1.57 ZFT = 2.55 MAr = 2.55 BAr = 2.50	2.36 (Least Misfit of all model scenarios) **Most Viable Model**

		Ma)		
	Model Scenario 2 (Two-time Activation)	MHT (26 Ma-0 Ma) MCT (21 Ma-20 Ma, 6.5 Ma-6.0 Ma) CNF (21Ma-20 Ma, 6.5 Ma-6.0 Ma) STDS (21Ma-20 Ma, 6.5 Ma-6.0 Ma)	AFT = 1.58 ZFT = 2.92 MAr = 3.16 BAr = 2.85	2.77
	Model Scenario 3 (Exclude MCT)	MHT (26Ma-0Ma) CNF (21Ma-20 Ma, 6.5 Ma-6.0 Ma) STDS (21Ma-20 Ma, 6.5 Ma-6.0 Ma)	AFT = 7.29 ZFT = 3.70 MAr = 2.46 BAr = 0.706	3.84
	Model Scenario 4 (STDS and CNF one-time activation)	MHT (26Ma-0Ma) MCT (21 Ma-20Ma) CNF (21Ma-20 Ma) STDS (21Ma-20 Ma)	AFT = 5.904 ZFT = 3.018 MAr = 2.044 BAr = 1.613	3.24
	Model Scenario 5 (CNF one-time activation)	MHT (26Ma-0Ma) MCT (21 Ma-20Ma) CNF (21Ma-20 Ma) STDS (21Ma-20 Ma, 6.5 Ma-6.0 Ma)	AFT = 3.81 ZFT = 2.25 MAr = 1.69 BAr = 2.12	2.47
	Model Scenario 6 (STDS one-time activation)	MHT (26Ma-0Ma) MCT (21 Ma-20Ma) CNF (21Ma-20	AFT = 4.23 ZFT = 3.04 MAr = 2.75 BAr = 2.31	3.054

		Ma, 6.5 Ma-6.0 Ma) STDS (21Ma-20 Ma)		
	Model Scenario 7 (Exclude MHT)	MCT (21Ma-20 Ma, 6.5 Ma-6.0 Ma) CNF (21Ma-20 Ma, 6.5 Ma-6.0 Ma) STDS (21Ma-20 Ma, 6.5 Ma-6.0 Ma)	AFT = 14.94 ZFT = 8.65 MAr = 5.07 BAr = 4.08	8.302
Gianbul Dome (Include Data from MCT to STDS) (AFT, ZFT, ZHe, MAR, BAR) (See Figs. S2b and S3h)	Model Scenario 8	MHT (26Ma-0Ma) MCT (22 Ma-21Ma, 10-8Ma, 6.02-5.9Ma, 3.11-3.25Ma) CNF (23Ma-22 Ma, 10.28-10.07Ma, 5.7-3.2Ma) STDS (21Ma-19 Ma, 6.9-5.9 Ma, 3.0-5.1Ma)	AFT = 2.326 ZFT = 3.032 ZHe = 2.927 MAr = 1.896 BAr = 2.636	2.578

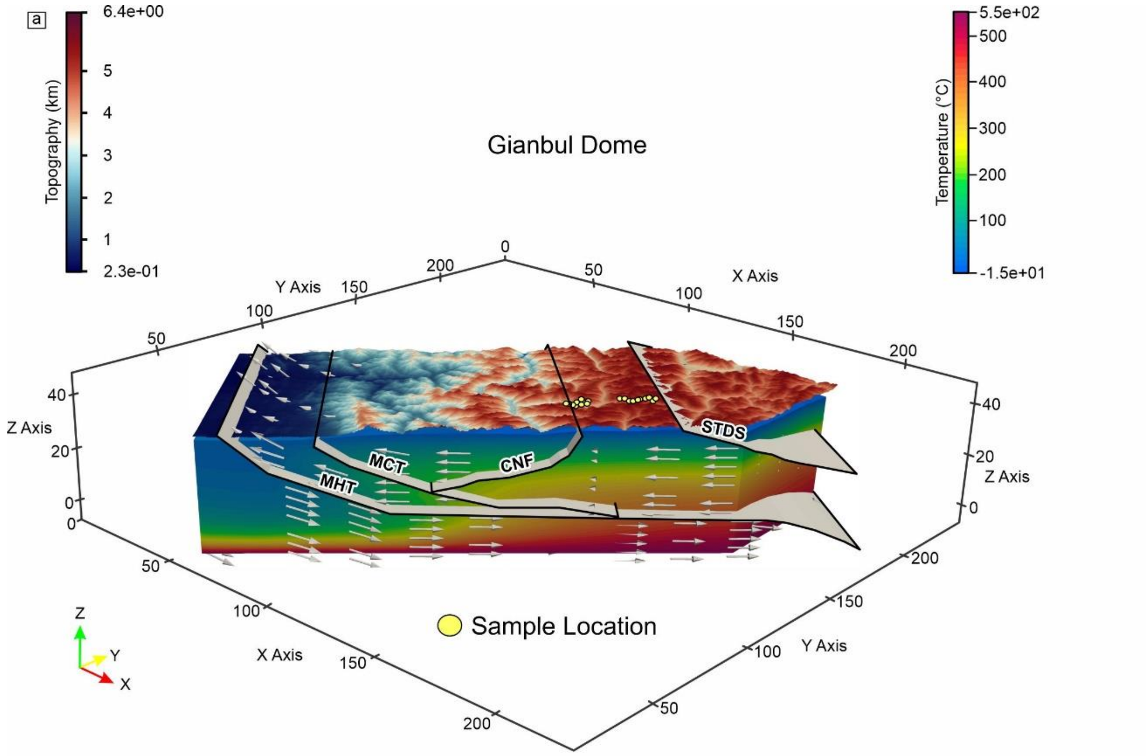
a
6.4e+00
5
4
3
2
1
2.3e-01
Topography (km)
Gianbul Dome
5.5e+02
500
400
300
200
100
-1.5e+01
Temperature (°C)
X Axis
Y Axis
Z Axis
MCT
CNF
MHT
STDS
Sample Location

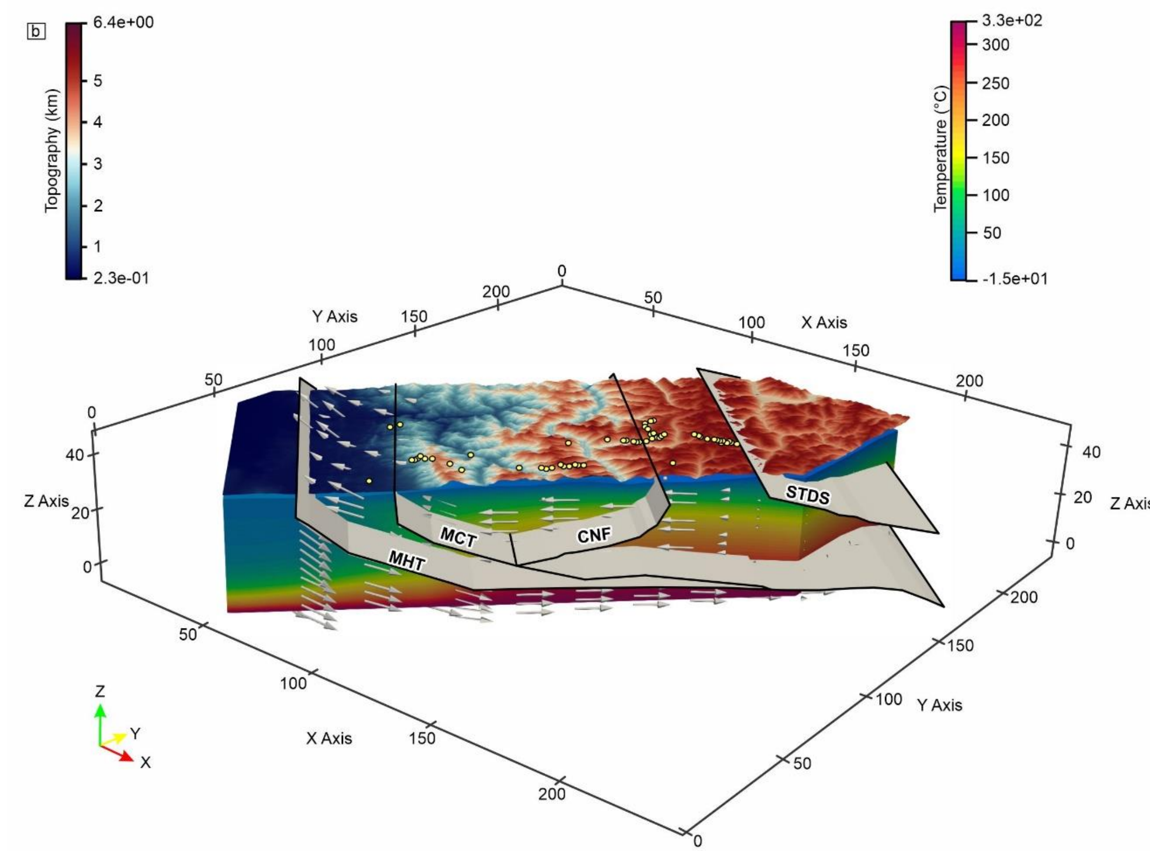
b
6.4e+00
5
4
3
2
1
2.3e-01
Topography (km)
3.3e+02
300
250
200
150
100
50
-1.5e+01
Temperature (°C)
X Axis
Y Axis
Z Axis
MCT
CNF
MHT
STDS

Fig. S2

Fig. S2: Figure (a,b) shows the 3D model for the Gianbul Dome, where isotherms and velocity vectors demonstrated in the cross-section are constrained after employing the Pecube Forward model.

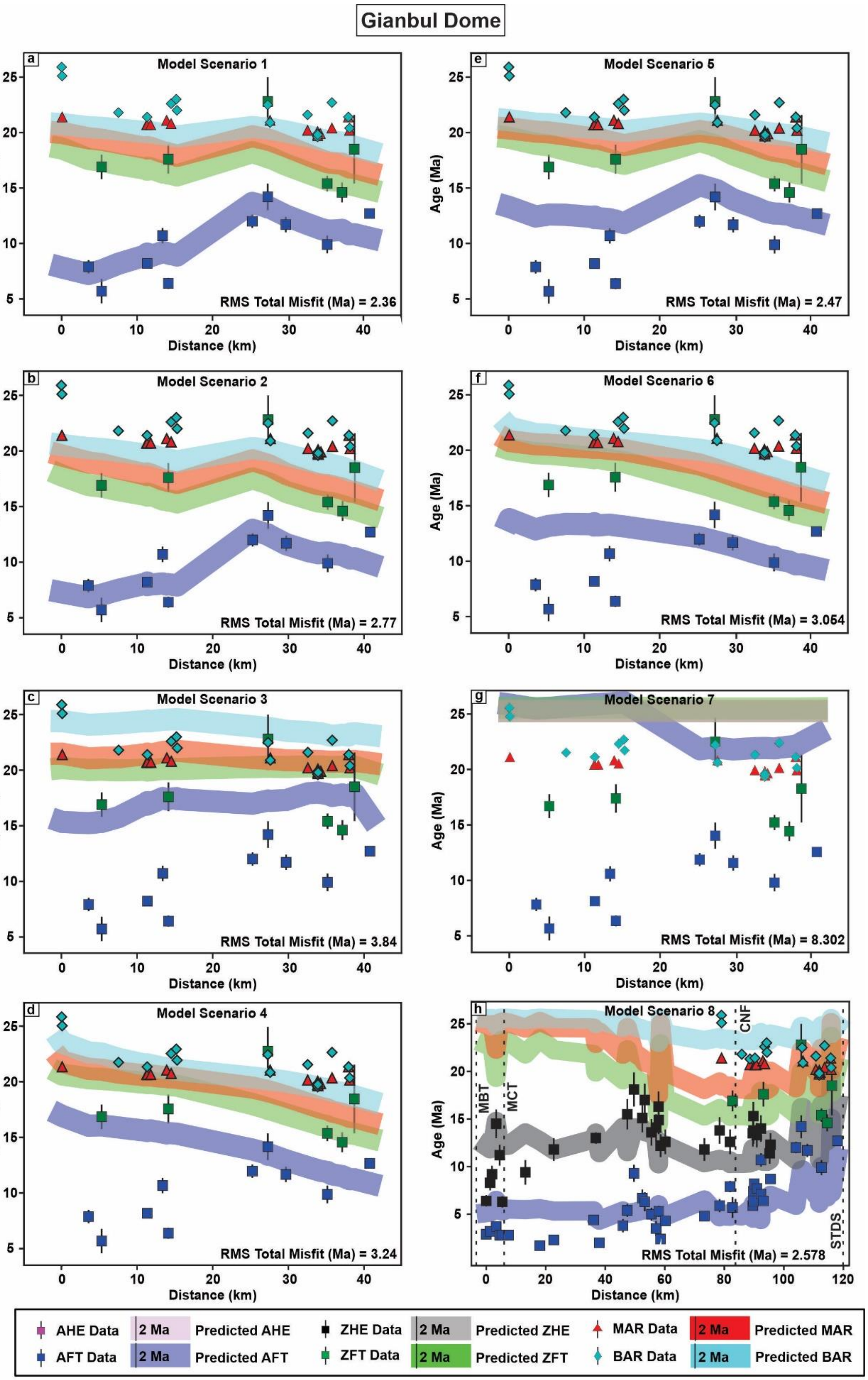

Gianbul Dome
a
Model Scenario 1
RMS Total Misfit (Ma) = 2.36
e
Model Scenario 5
RMS Total Misfit (Ma) = 2.47
b
Model Scenario 2
RMS Total Misfit (Ma) = 2.77
f
Model Scenario 6
RMS Total Misfit (Ma) = 3.054
c
Model Scenario 3
RMS Total Misfit (Ma) = 3.84
g
Model Scenario 7
RMS Total Misfit (Ma) = 8.302
d
Model Scenario 4
RMS Total Misfit (Ma) = 3.24
h
Model Scenario 8
MBT
MCT
CNF
STDS
RMS Total Misfit (Ma) = 2.578
Age (Ma)
Distance (km)
AHE Data
2 Ma
Predicted AHE
AFT Data
2 Ma
Predicted AFT
ZHE Data
2 Ma
Predicted ZHE
ZFT Data
2 Ma
Predicted ZFT
MAR Data
2 Ma
Predicted MAR
BAR Data
2 Ma
Predicted BAR

Fig. S3

Fig. S3: Figures a-h illustrate the age distance plot for the observed and predicted for Gianbul domes in the Himalaya after Pecube forward models.

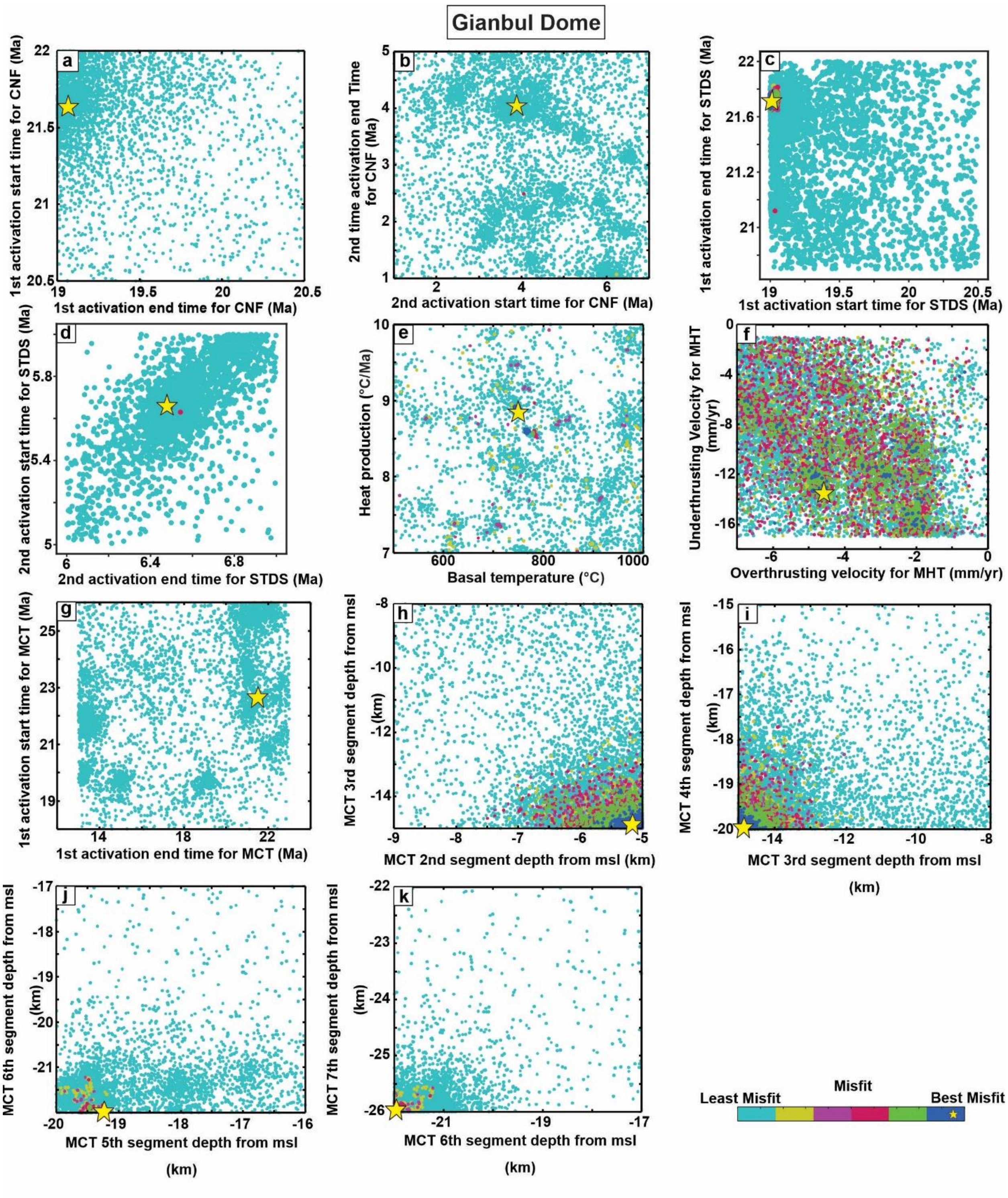

Fig. S4

Fig. S4: Figures a-k show the results of inverse model plots for different parameters for the Gianbul Dome, where the yellow star mark represents the best fit.

2.3.1.1 Field Evidence

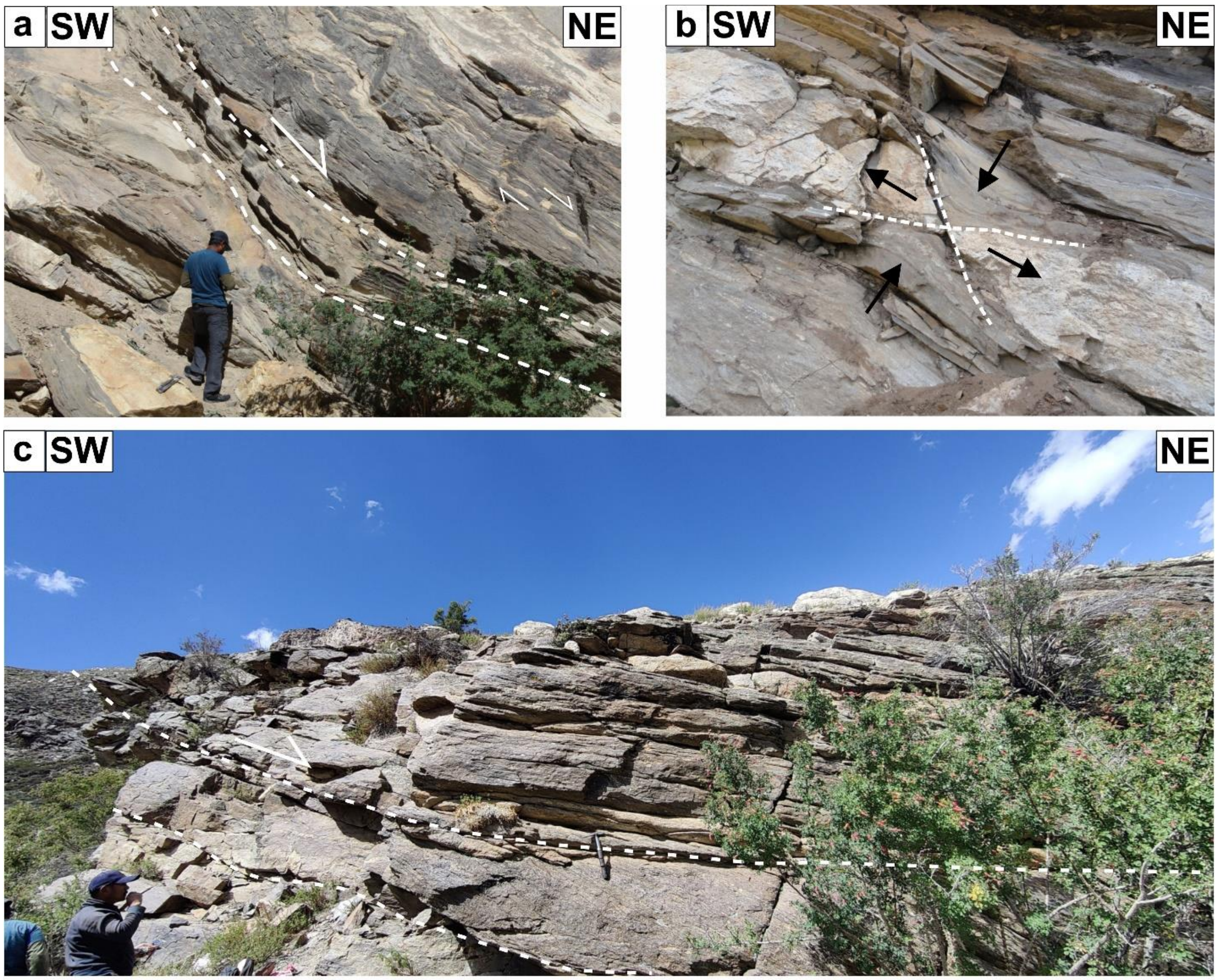

Fig. S5

Fig. S5: Figures a-c illustrates the concave upward structure of the Gianbul Dome.

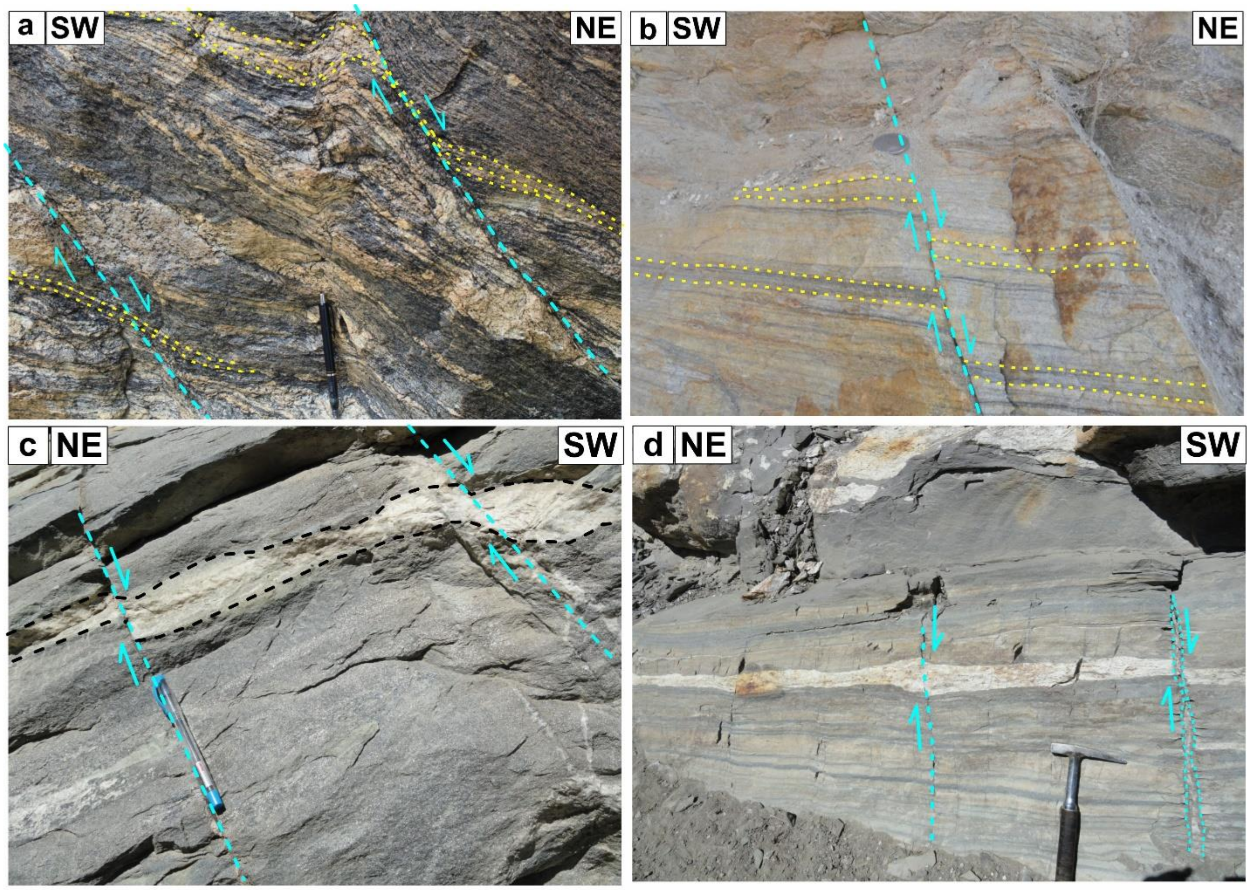

Fig. S6

Fig. S6: Figures a-d illustrate the Normal fault brittle deformation structure of the Gianbul Dome.

2.3.1.2 Ksn for Gianbul Dome

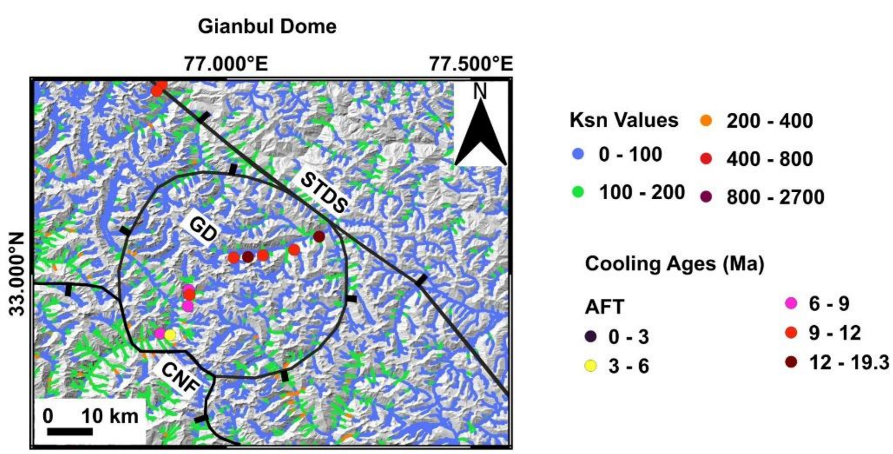

Fig. S7

Fig. S7: The Figure shows the Ksn results with the youngest cooling ages at Gianbul Dome.

2.3.2 Suru Dome

For Suru Dome, we used three faults to simulate the 3D forward model, which has a thickness of 35 km, with nx being 10616 and ny being 8564, where two faults were modeled into thrust faults (MHT and MCT), and two fault was modeled as a normal fault (CNF and STDS) to incorporate the cooling ages (AFT, ZFT and BAr), and different parameters data used given in Supplementary Tables S3 and S4. Our modeling technique encompasses two-step tectonomorphic scenarios using Richard Ketcham's routine for synthetic age prediction. The fault data was obtained from (Hazarika et al., 2017), and the MCT fault data is the inverse model data. We modeled the CNF and STDS as a normal fault in two time scenarios (from ~21 Ma to ~20 Ma for the first scenario and from ~6.5 Ma to ~4 Ma for the second scenario), whereas MCT was modeled as a thrust for the time step between ~22 Ma to ~19 Ma. We took a second-step scenario for MCT, but it had minimal effects on the predicted data (See the table below), while MHT was considered a thrust fault that was active between ~23 Ma to the present time. In the forward model, we did not account for the relationship between age and elevation; instead, we measured the misfit weight to determine the difference between observed and predicted cooling ages. The forward model's result, with a best RMS misfit of 2.183 Ma, is displayed in supplementary Fig. S8 and Fig. S9(a-f), whereas the inverse model's result is shown in supplementary Fig. S10 (a-e). After forward modeling, we employed the inverse modeling using the neighborhood algorithm using Pecube, which has ranges and best fits, as given in supplementary Table S4.

The table below shows the number of model scenario tests to constrain the best RMS misfit.

Dome Names	Faults	Fault Parameters Used	RMS Misfit (Ma)	RMS Total Misfit (Ma)
	Model Scenario	MHT (23Ma-	AFT = 1.584	2.183

Suru Dome	1 (Two-time Activation)	0Ma) MCT (21.95 Ma-19.72 Ma, 6.5 Ma – 6 Ma) CNF (21Ma-20 Ma, 6.5 Ma-6.0 Ma) STDS (20.95 Ma-19.82 Ma, 6.2 Ma - 4.32 Ma)	ZFT = 2.191 BAr = 4.614	**Most Viable Model**
	Model Scenario 2 (Except MCT 2nd activation)	MHT (23Ma-0Ma) MCT (21.95 Ma-19.72 Ma) CNF (21Ma-20 Ma, 6.5 Ma-6.0 Ma) STDS (20.95 Ma-19.82 Ma, 6.2 Ma - 4.32 Ma)	AFT = 1.57 ZFT = 2.74 BAr = 4.59	2.194
	Model Scenario 3 (Exclude MCT)	MHT (23Ma-0Ma) CNF (21Ma-20 Ma, 6.5 Ma-6.0 Ma) STDS (20.95 Ma-19.82 Ma, 6.2 Ma - 4.32 Ma	AFT = 1.56 ZFT = 2.76 BAr = 4.621	2.199
	Model Scenario 4 (STDS and CNF one-time activation)	MHT (23Ma-0Ma) MCT (21.95 Ma-19.72 Ma) CNF (21Ma-20 Ma) STDS (20.95 Ma-19.82 Ma)	AFT = 1.925 ZFT = 3.656 BAr = 2.199	2.432
	Model Scenario 5 (CNF one-time activation)	MHT (26Ma-0Ma) MCT (21 Ma-20Ma)	AFT = 2.007 ZFT = 3.275 BAr = 4.167	2.413

		CNF (21Ma-20 Ma) STDS (20.95 Ma-19.82 Ma, 6.2 Ma - 4.32 Ma)		
	Model Scenario 6 (STDS one-time activation)	MHT (23Ma-0Ma) MCT (21.95 Ma-19.72 Ma, 6.5 Ma – 6 Ma) CNF (21Ma-20 Ma, 6.5 Ma-6.0 Ma) STDS (20.95 Ma-19.82 Ma)	AFT = 1.681 ZFT = 3.106 BAr = 4.479	2.253

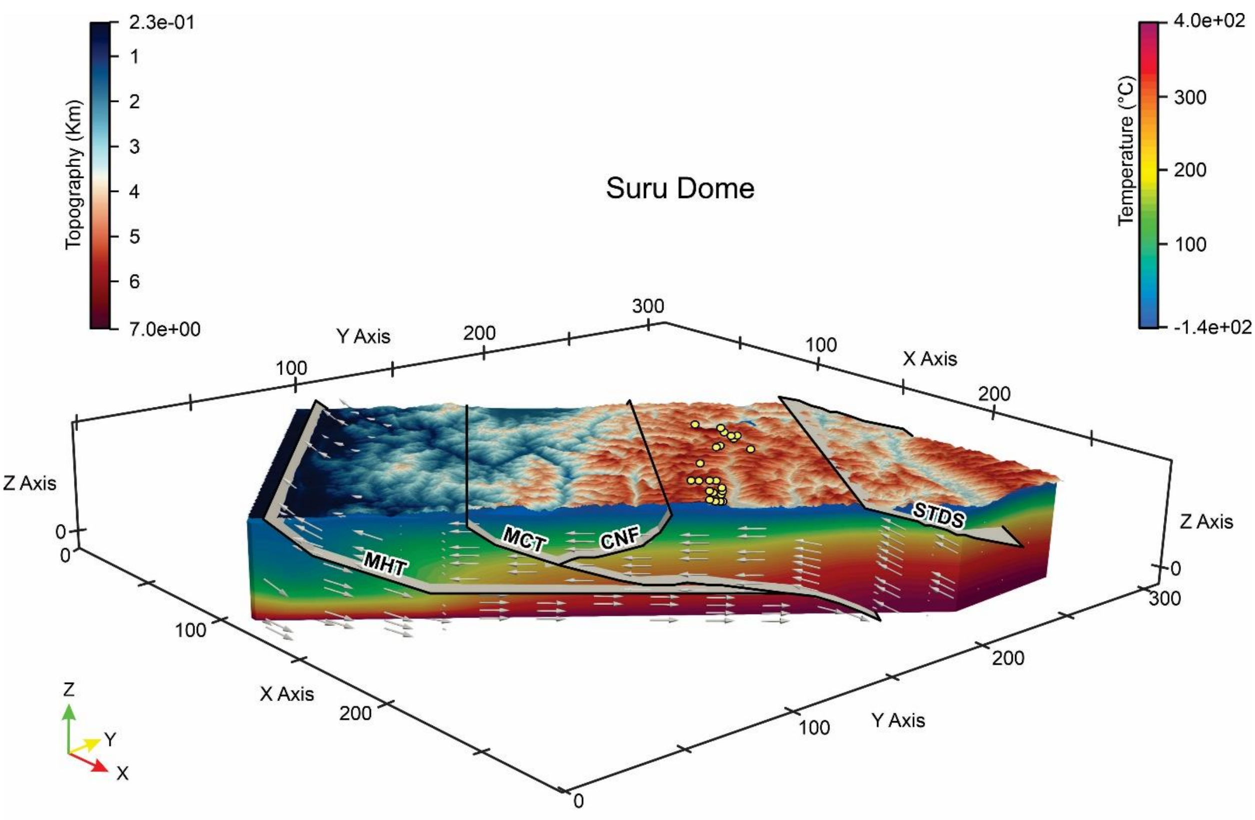

Fig. S8

Fig. S8: The figure shows the 3D model for the Suru Dome, where isotherms and velocity vectors demonstrated in the cross-section are constrained after employing the Pecube Forward model.

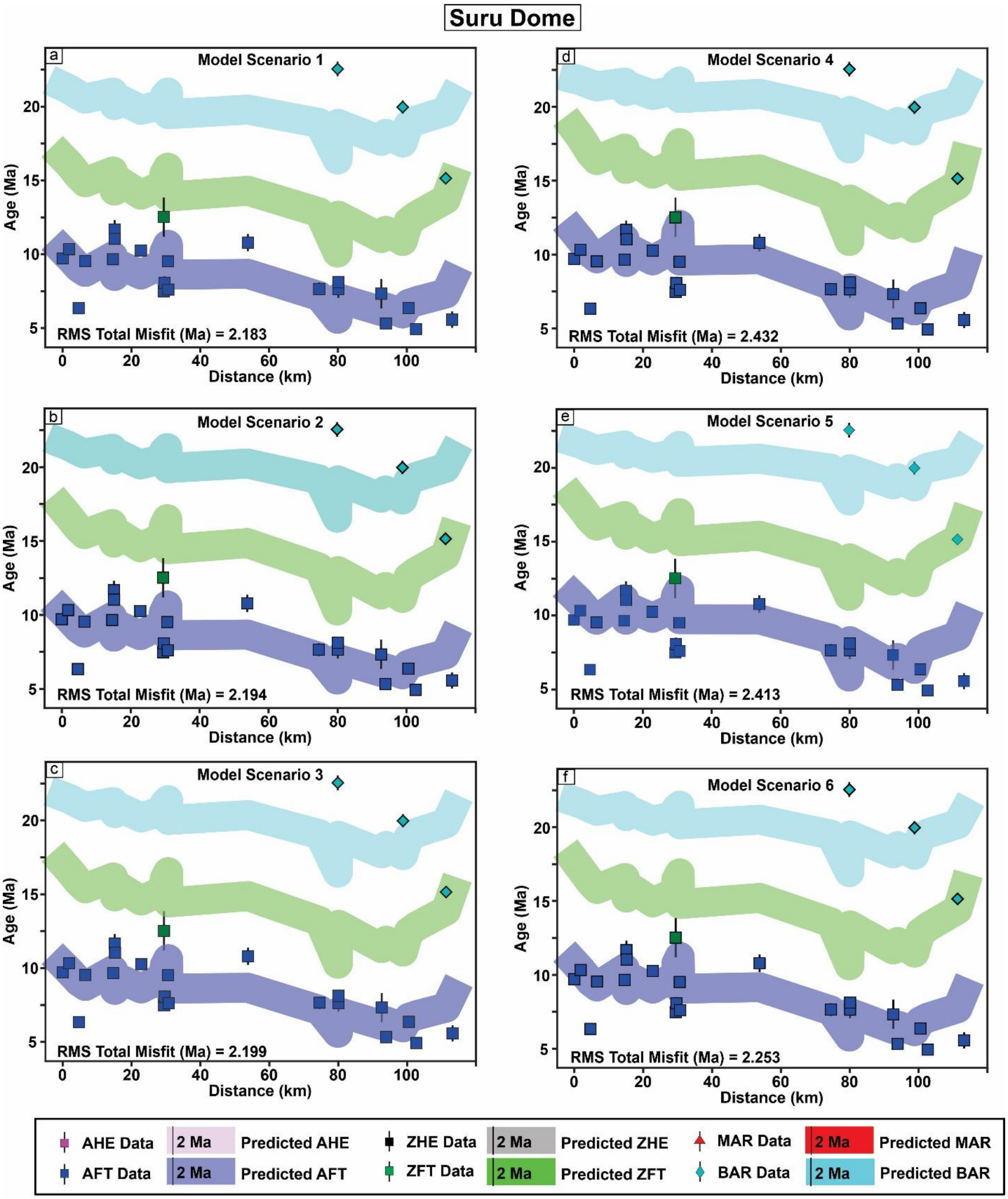

Fig. S9

Fig. S9: Figures a-f illustrate the age distance plot for the observed and predicted for Suru dome in the Himalaya after Pecube forward models.

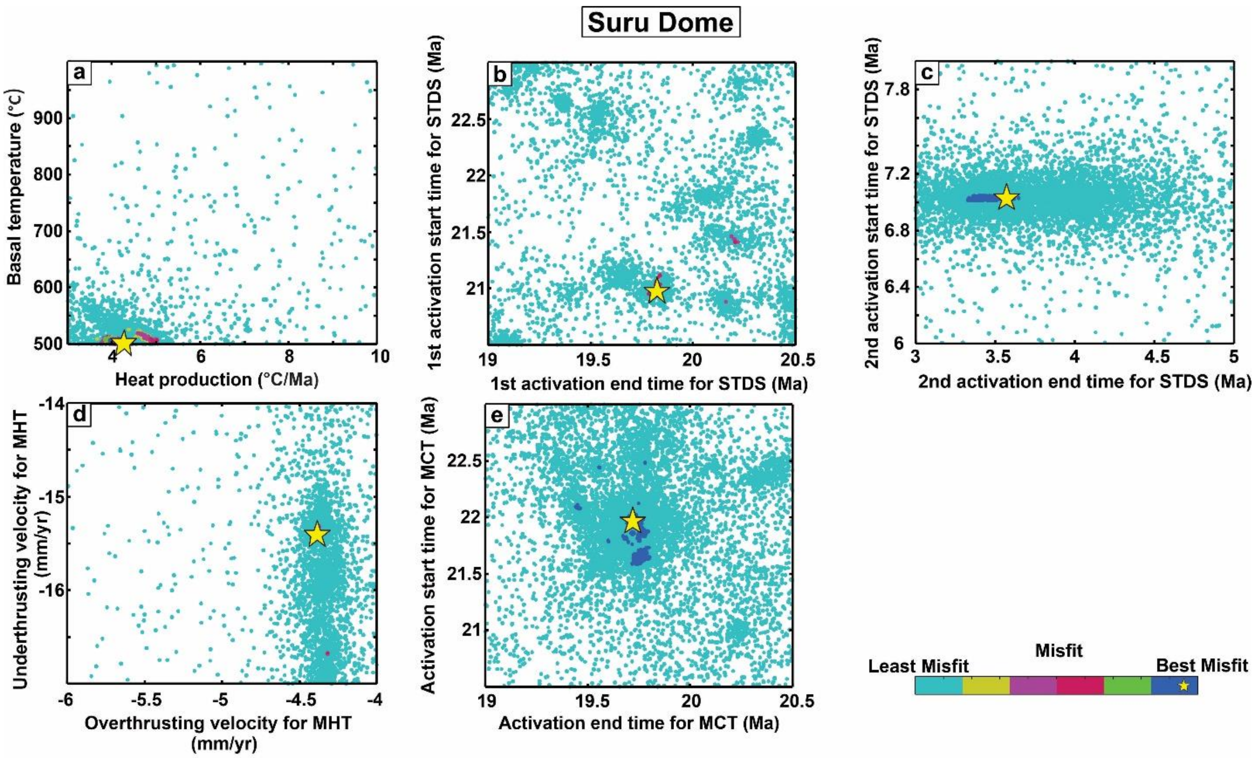

Fig. S10

Fig. S10: Figures a-e show the results of the inverse model for different parameters for the Suru Dome, where the yellow star mark represents the best fit.

2.3.3 Chisoti Dome

For the Chisoti dome, we considered the 3D model to have a thickness of 35 km where nx is 10616 and ny is 8564, from 23.7 Ma to the present time scenario using the Richard Ketcham routine for 3D modeling, where we used two types of cooling ages, AFT, ZFT, and BAr, which are given in the supplementary Table S1a. Among different parameters, we did not consider the age elevation case (overpredicting the synthetic cooling ages), shear heating, or isostasy case in our model (Herman et al., 2010). To simulate the above scenario, we used four fault data sets

(MHT, CNF, MCT, and STDS). Among four faults, MHT and STDS were taken from Hazarika et al., 2017, CNF from Yadav et al., 2016, and MCT structures obtained after inverse modeling, while MHT was considered a thrust fault active from 23.7 Ma to the present time, and for the CNF fault, we used two-time scenarios, 19.8-18 Ma and 6.10-3.9 Ma. Likewise, STDS is also modeled as a normal fault for two-time steps, which are between 20.9-19.2 Ma and 6.5-6 Ma. In contrast, the MCT modeled as a thrust fault is considered a one-time step during the ductile deformation between 21.0 and 19.2 Ma. The remaining parameters used in the inverse modeling are provided in Supplementary Table S4. The forward model's result, with a best RMS misfit of 3.0107 Ma (supplementary Fig. S11 and Fig. S12 (a-f)). After forward modeling, we employed the inverse modeling using the neighborhood algorithm using Pecube, which has the misfit, as given in supplementary Fig. S13 (a-h).

The table below shows the number of model scenario tests to constrain the best RMS misfit.

Dome Names	Faults	Fault Parameters Used	RMS Misfit (Ma)	RMS Total Misfit (Ma)
Chisoti Dome	Model Scenario 1 (Two-time Activation)	MHT (23.7 Ma-0Ma) MCT (21 Ma-19.2 Ma, 6.5 Ma - 6 Ma) CNF (19.8Ma-18 Ma, 6.1 Ma-3.9 Ma) STDS (20.9 Ma-19.2 Ma, 6.5 Ma - 6 Ma)	AFT = 1.869 ZFT = 4.425 BAr = 4.318	3.0107 **Most Viable Model**
	Model Scenario 2 (Except MCT 2nd activation)	MHT (23.7 Ma-0Ma) MCT (21 Ma-19.2 Ma) CNF (19.8Ma-18 Ma, 6.1 Ma-3.9 Ma)	AFT = 1.866 ZFT = 4.896 BAr = 4.044	3.058

		STDS (20.9 Ma-19.2 Ma, 6.5 Ma - 6 Ma)		
	Model Scenario 3 (Exclude MCT)	MHT (23.7 Ma-0Ma) CNF (19.8Ma-18 Ma, 6.1 Ma-3.9 Ma) STDS (20.9 Ma-19.2 Ma, 6.5 Ma - 6 Ma)	AFT = 1.87 ZFT = 4.85 BAr = 4.036	3.045
	Model Scenario 4 (STDS and CNF one-time activation)	MHT (23.7 Ma-0Ma) MCT (21 Ma-19.2 Ma) CNF (19.8Ma-18 Ma) STDS (20.9 Ma-19.2 Ma)	AFT = 14.00 ZFT = 10.928 BAr = 5.809	12.343
	Model Scenario 5 (CNF one-time activation)	MHT (23.7 Ma-0Ma) MCT (21 Ma-19.2 Ma) CNF (19.8Ma-18 Ma) STDS (20.9 Ma-19.2 Ma, 6.5 Ma - 6 Ma)	AFT = 12.067 ZFT = 10.365 BAr = 4.776	10.764
	Model Scenario 6 (STDS one-time activation)	MHT (23.7 Ma-0Ma) MCT (21 Ma-19.2 Ma) CNF (19.8Ma-18 Ma, 6.1 Ma-3.9 Ma) STDS (20.9 Ma-19.2 Ma)	AFT = 1.848 ZFT = 7.256 BAr = 3.422	3.633

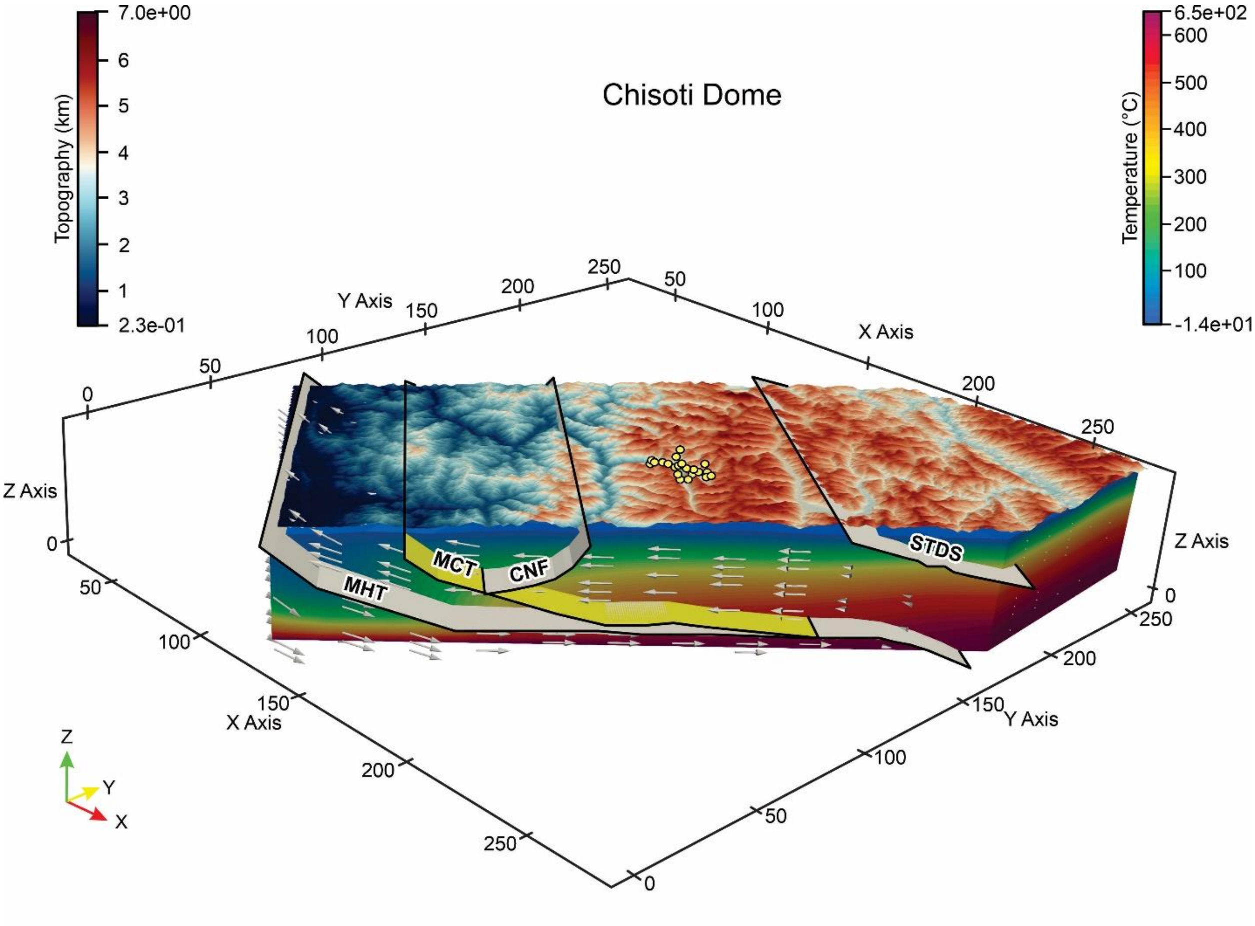

Fig. S11

Fig. S11: The figure shows the 3D model for the Chisoti Dome, where isotherms and velocity vectors demonstrated in the cross-section are constrained after employing the Pecube Forward model.

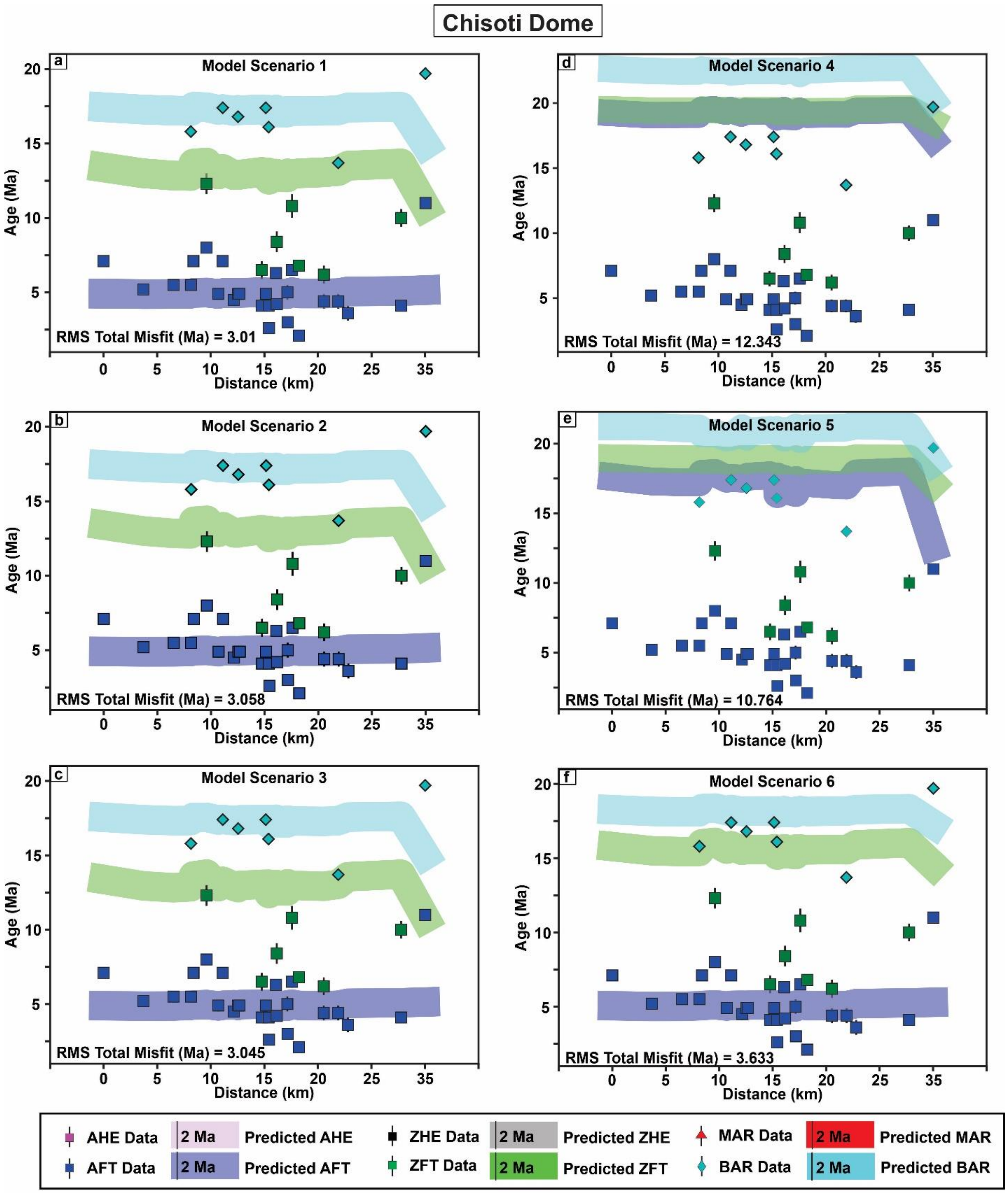
Chisoti Dome
Model Scenario 1
RMS Total Misfit (Ma) = 3.01
Model Scenario 2
RMS Total Misfit (Ma) = 3.058
Model Scenario 3
RMS Total Misfit (Ma) = 3.045
Model Scenario 4
RMS Total Misfit (Ma) = 12.343
Model Scenario 5
RMS Total Misfit (Ma) = 10.764
Model Scenario 6
RMS Total Misfit (Ma) = 3.633
Age (Ma)
Distance (km)
AHE Data
2 Ma
Predicted AHE
AFT Data
Predicted AFT
ZHE Data
Predicted ZHE
ZFT Data
Predicted ZFT
MAR Data
Predicted MAR
BAR Data
Predicted BAR

Fig. S12

Fig. S12: Figures a-f illustrate the age distance plot for the observed and predicted for Chisoti domes in the Himalaya after Pecube forward models.

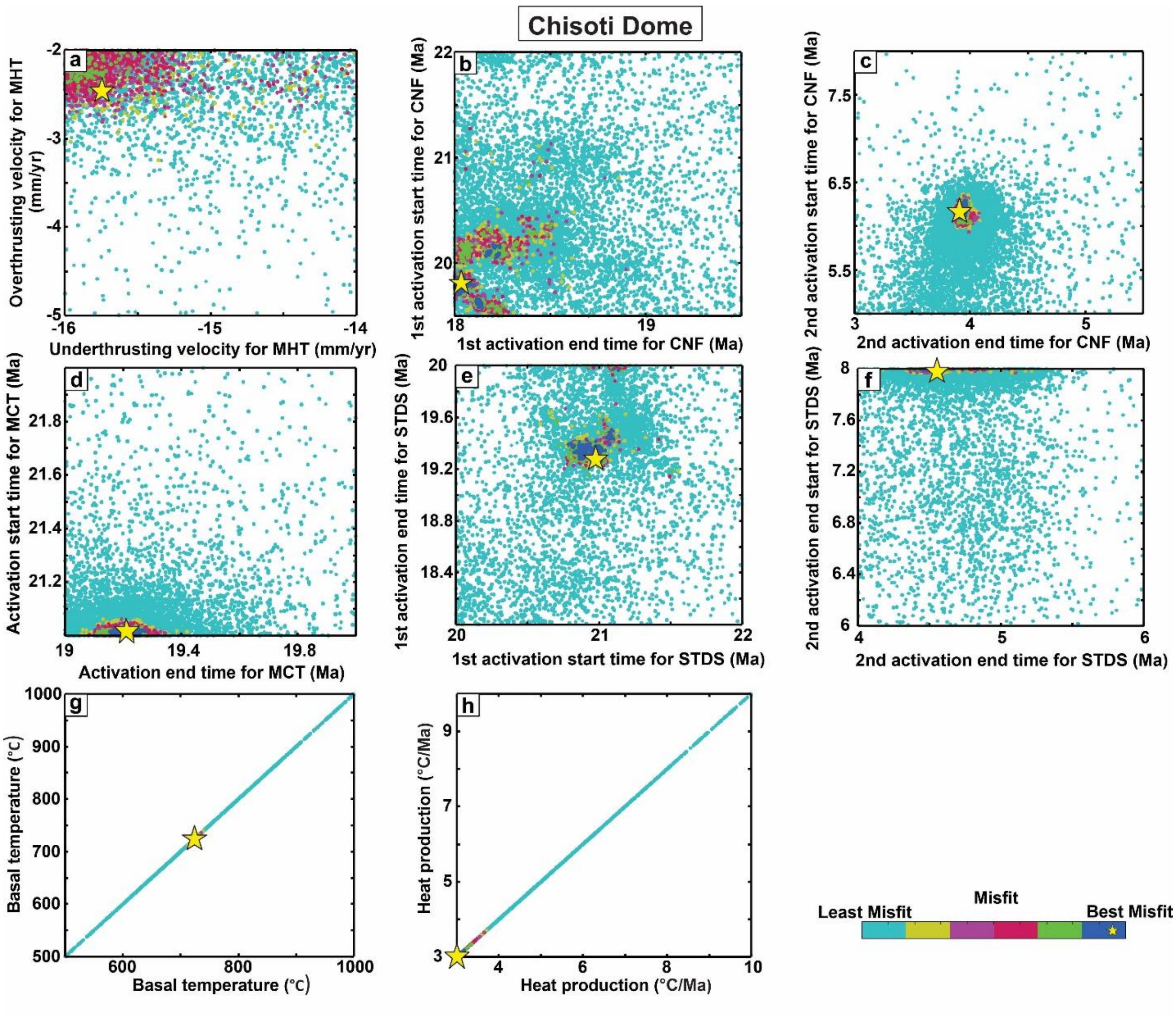

Fig. S13

Fig. S13: Figures a-h show the results of inverse model plots for different parameters for the Chisoti Dome, where the yellow star mark represents the best fit.

2.3.4 Changgo-Malashan Dome

A 3D model for the Changgo Dome and Malashan Dome, which is located in South Central

Tibet, was simulated for two tectonic scenarios since 22 Ma has a model thickness of 60 km and utilizes three type of cooling ages, AFT, MAr and BAr, where Richard Ketcham Routine was employed to construct the 3D model, where isostasy and shear heating parameters were not considered (Herman et al., 2010). To simulate the Model, we employed three fault data, MHT, MCT, and STDS, which were obtained (Acton et al., 2011; Grujic et al., 2011; Lee et al., 2000; Mitra et al., 2005; Warren et al., 2011; Zhao et al., 1993). Among three faults, MHT was modeled as an active thrust fault during the period from 22 million years ago to the present day, while STDS was recognized as a normal fault during two distinct time steps: from 17.43 to 17.41 million years ago and from 16.85 to 13.84 million years ago. The MCT is considered a thrust fault from 21-20 Ma. The result of the forward model, consisting of the best RMS misfit, is 2.027 Ma (supplementary Fig. S14, S15(a-d)). The Pecube was used to predict the age of brittle deformation, and inverse modeling (neighborhood algorithm using Pecube) was utilized to determine the activation time for this dome, which has ranges and misfits, as given in supplementary Table S4 and inverse result displayed in supplementary Fig. S16 (a-d).

The table below shows the number of model scenario tests to constrain the best RMS misfit.

Dome Names	Faults	Fault Parameters Used	RMS Misfit (Ma)	RMS Total Misfit (Ma)
Changgo and Malashan Domes	Model Scenario 1	MHT (22Ma-0Ma) STDS (17.43 Ma-17.41 Ma, 16.85 Ma – 13.87 Ma)	ZFT = 1.804 MAr = 2.002 BAr = 2.363	2.027 **Most Viable Model**
	Model Scenario 2 (STDS active one time)	MHT (22Ma-0Ma) STDS (17.43 Ma-17.41 Ma)	ZFT = 2.393 MAr = 1.946 BAr = 2.02	2.121
	Model Scenario 3	MHT (22Ma-0Ma)	ZFT = 1.760 MAr = 2.03	2.233

	(With MCT)	STDS (17.43 Ma-17.41 Ma, 16.85 Ma – 13.87 Ma) MCT (21-20 Ma)	BAr = 3.089	
	Model Scenario 4 (Without MHT)	STDS (17.43 Ma-17.41 Ma, 16.85 Ma – 13.87 Ma) MCT (21-20 Ma)	ZFT = 3.102 MAr = 2.019 BAr = 3.0132	2.659

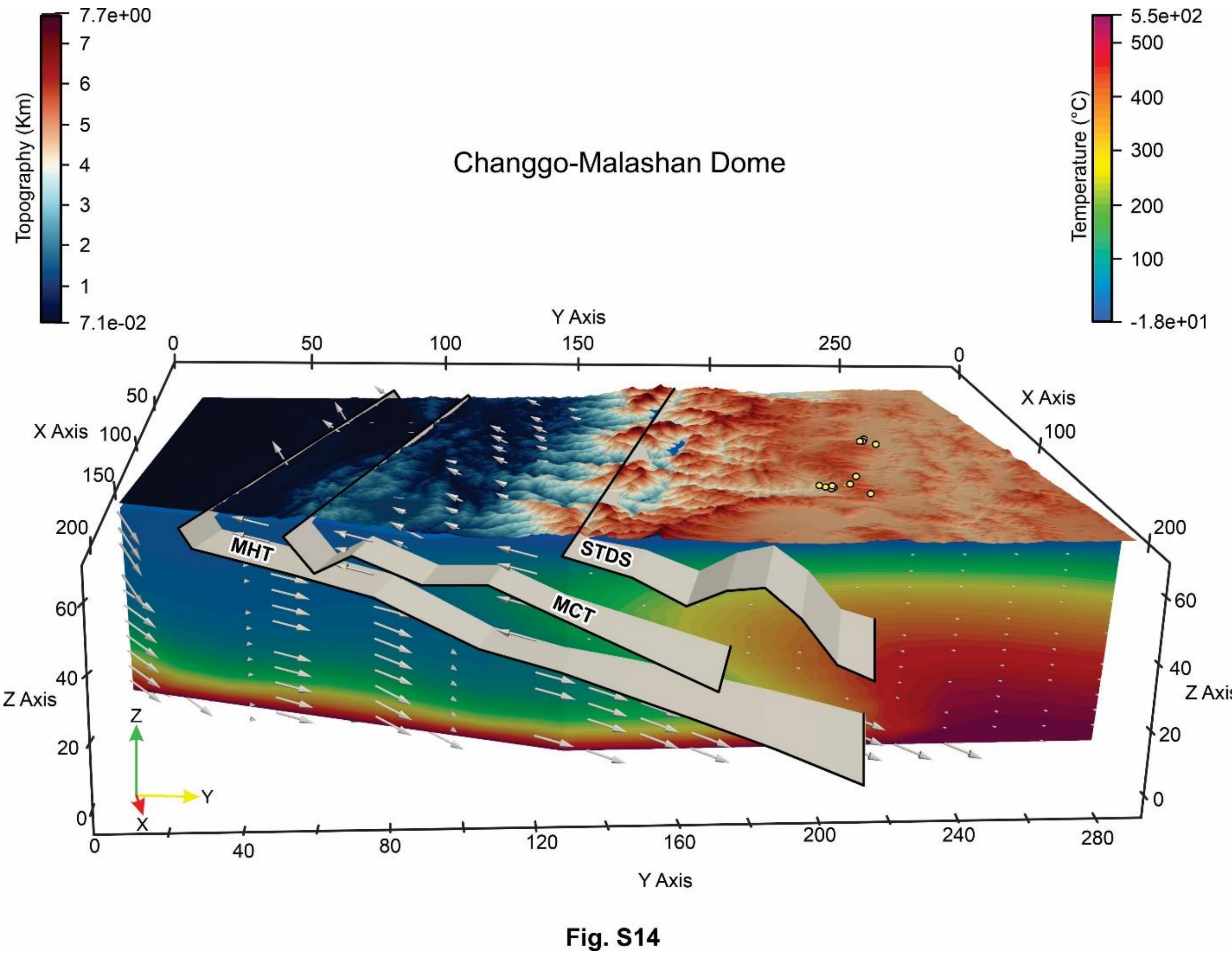

Fig. S14: The Figure shows the 3D model for the Changgo-Malashan Dome, where isotherms and velocity vectors demonstrated in the cross-sections are constrained after employing the Pecube Forward model.

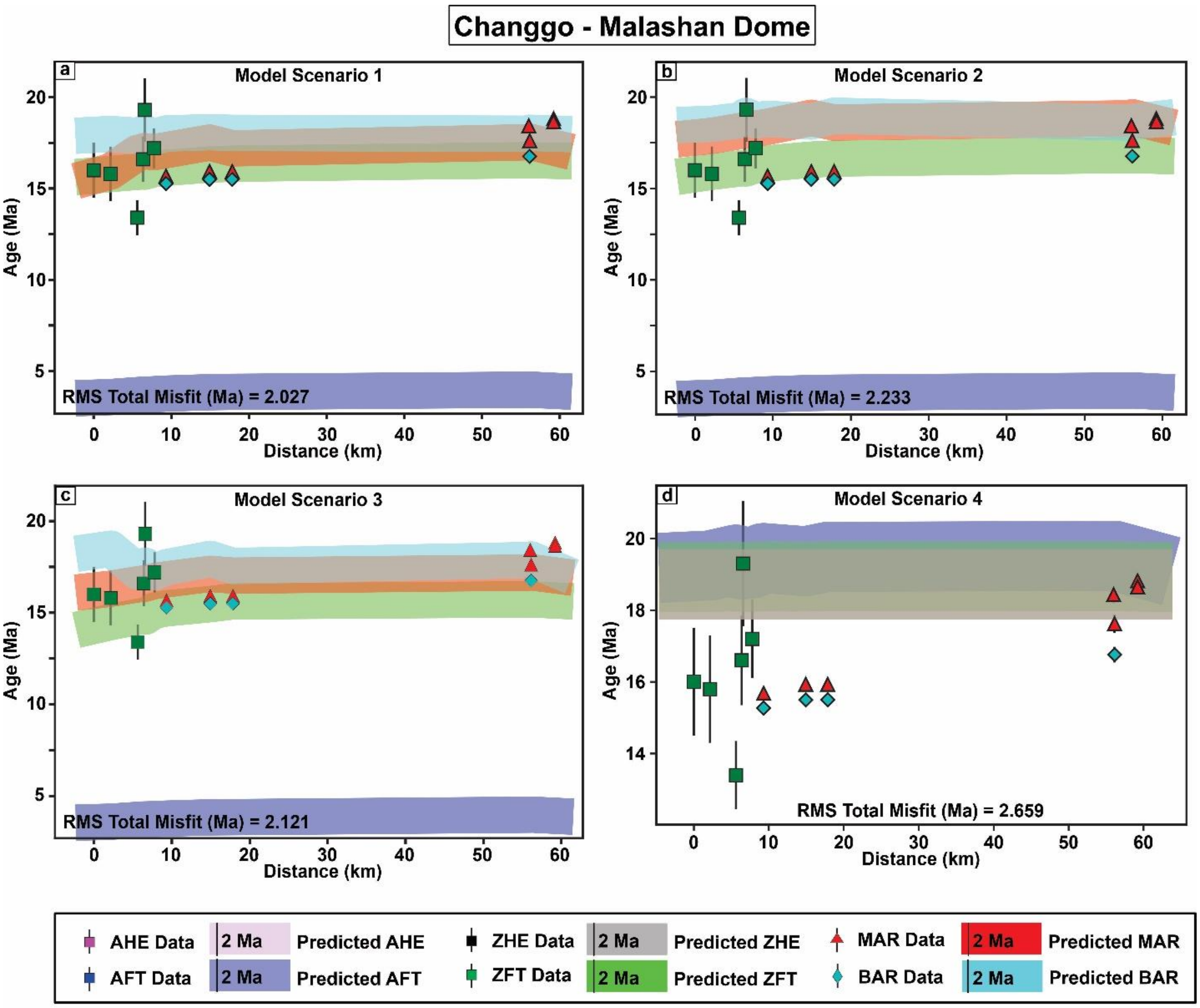

Fig. S15

Fig. S15: Figures a-d illustrate the age distance plot for the observed and predicted for Changgo-Malashan Dome in the Himalaya after Pecube forward models.

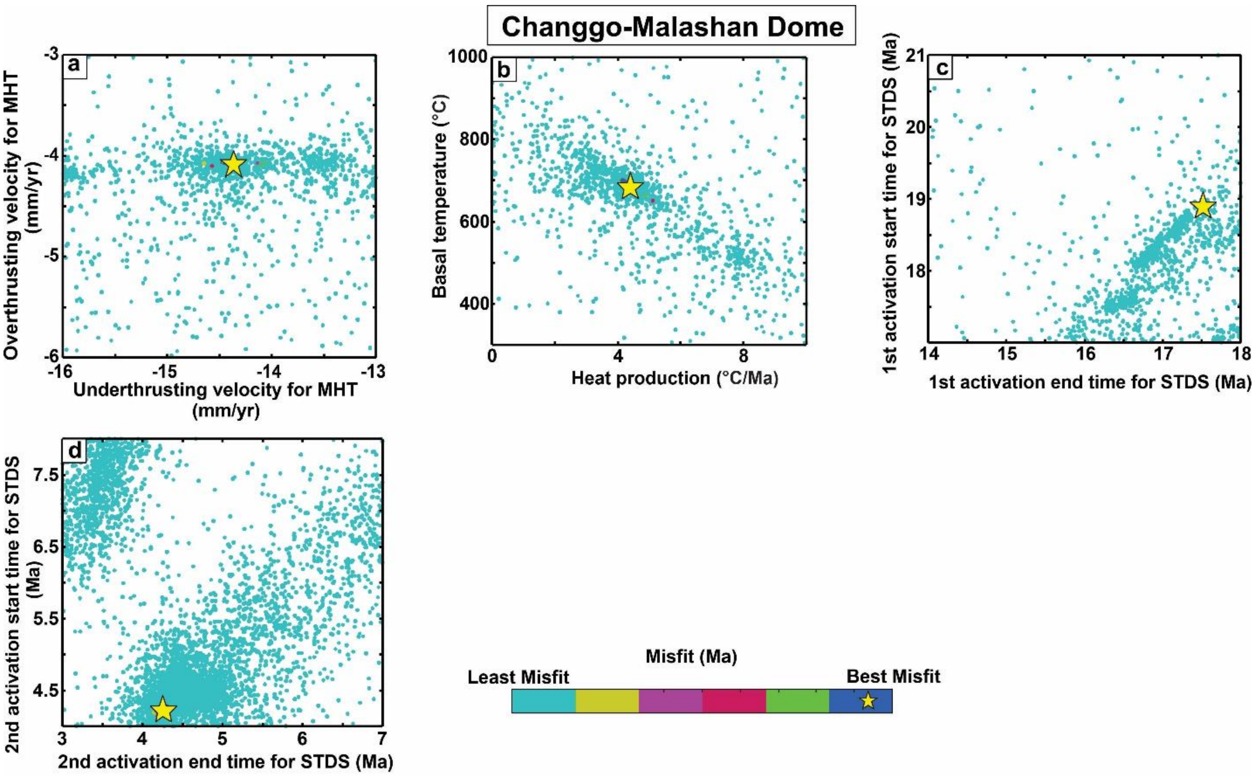

Fig. S16

Fig. S16: Figures a-d show the results of inverse model plots for different parameters for the Changgo-Malashan Dome, where the yellow star mark represents the best fit.

2.3.5 Mabja Dome

A 3D model of the Mabja dome was generated using a crustal thickness of 35 km, with dimensions of nx 4940 and ny 11838 for a two-time tectonic scenario modeled from 17 Ma to the present time because all cooling ages are younger than 17 Ma, where the shear heating, age elevation relationship, and isostasy parameters were not considered for modeling the Mabja dome. However, the Richards Ketcham Routine was used to model MBD and utilize three types of cooling ages: MAr, BAr, and AFT. The fault parameters used in this study were obtained from (Acton et al., 2011; Grujic et al., 2011; Lee et al., 2000; Mitra et al., 2005; Warren et al., 2011; Zhao et al., 1993), where three faults were considered: the MHT, MCT, and the STDS. The MHT was modeled as a thrust fault and has been active since 17 Ma. On the other hand, the STDS was modeled as a normal fault and was active during two time steps: from 15 to 14 million years ago and from 6.5 to 6 million years ago (supplementary Fig. S17, S18a-d), while the MCT was active as a thrust fault from 21 to 20 Ma. To accurately determine the time of activation, an inverse model was used, and the resulting outcomes are presented in Supplementary Table S4, and the inverse result is displayed in Supplementary Fig. S19 (a-f).

The table below shows the number of model scenario tests to constrain the best RMS misfit.

Dome Names	**Faults**	**Fault Parameters Used**	**RMS Misfit (Ma)**	**RMS Total Misfit (Ma)**
Mabja Dome	Model Scenario 1 All faults	MHT (17Ma-0Ma) STDS (15 Ma-14 Ma, 6.5 Ma – 6 Ma) MCT (21-20 Ma)	AFT = 2.725 MAr = 1.80 BAr = 2.243	2.206 **Most Viable Model**
	Model Scenario 2 (STDS active one time)	MHT (17Ma-0Ma) STDS (15 Ma-14 Ma) MCT (21-20 Ma)	AFT = 9.670 MAr = 4.879 BAr = 1.626	5.989
	Model Scenario 3 (Without MCT)	MHT (17Ma-0Ma) STDS (15 Ma-14 Ma, 6.5 Ma – 6 Ma)	AFT = 2.725 MAr = 1.805 BAr = 2.243	2.206
	Model Scenario 4 (Without MHT)	STDS (15 Ma-14 Ma, 6.5 Ma – 6 Ma) MCT (21-20 Ma)	AFT = 8.318 MAr = 2.757 BAr = 2.463	4.558

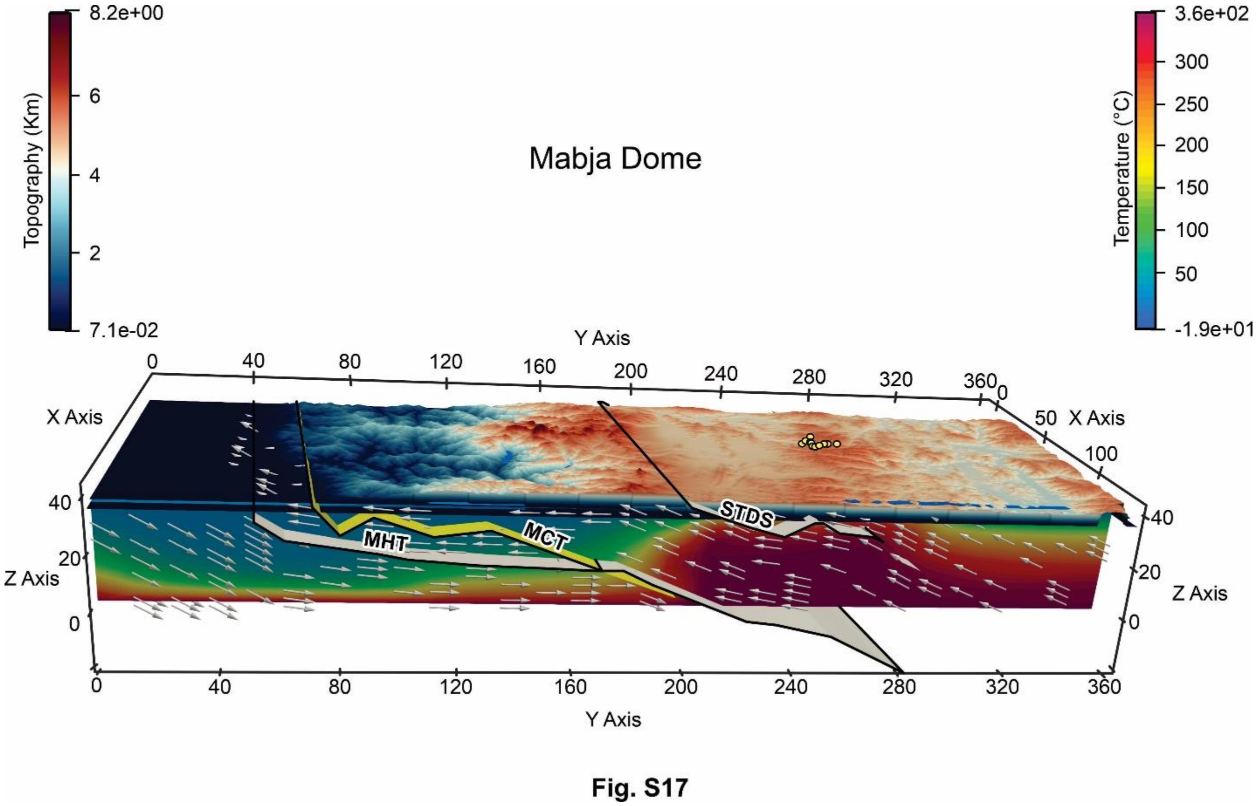

Fig. S17

Fig. S17: The Figure shows the 3D model for the Mabja Dome, where isotherms and velocity vectors demonstrated in the cross-sections are constrained after employing the Pecube Forward model.

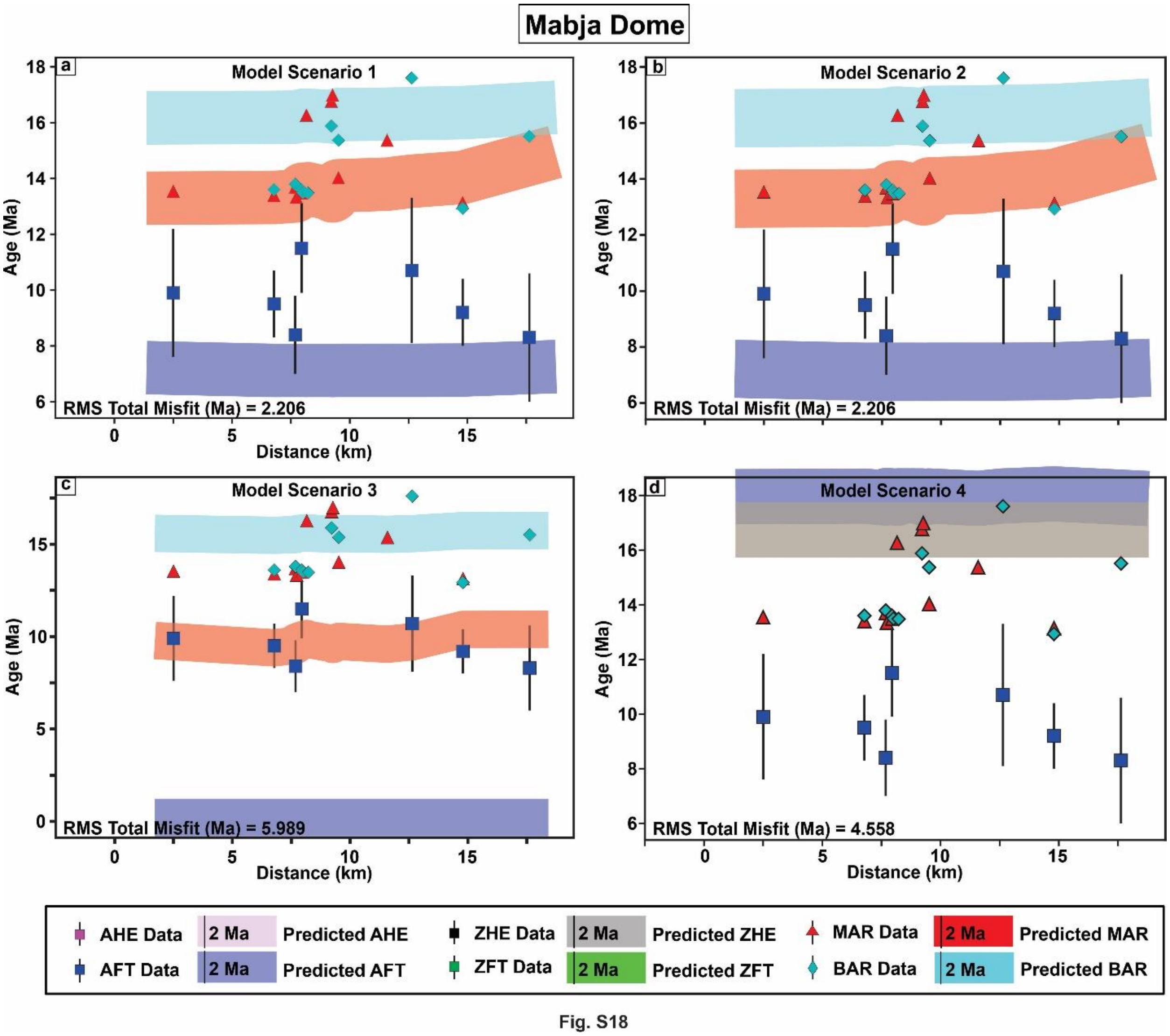

Fig. S18: Figures a-d illustrate the age distance plot for the observed and predicted for Mabja Dome in the Himalaya after Pecube forward models.

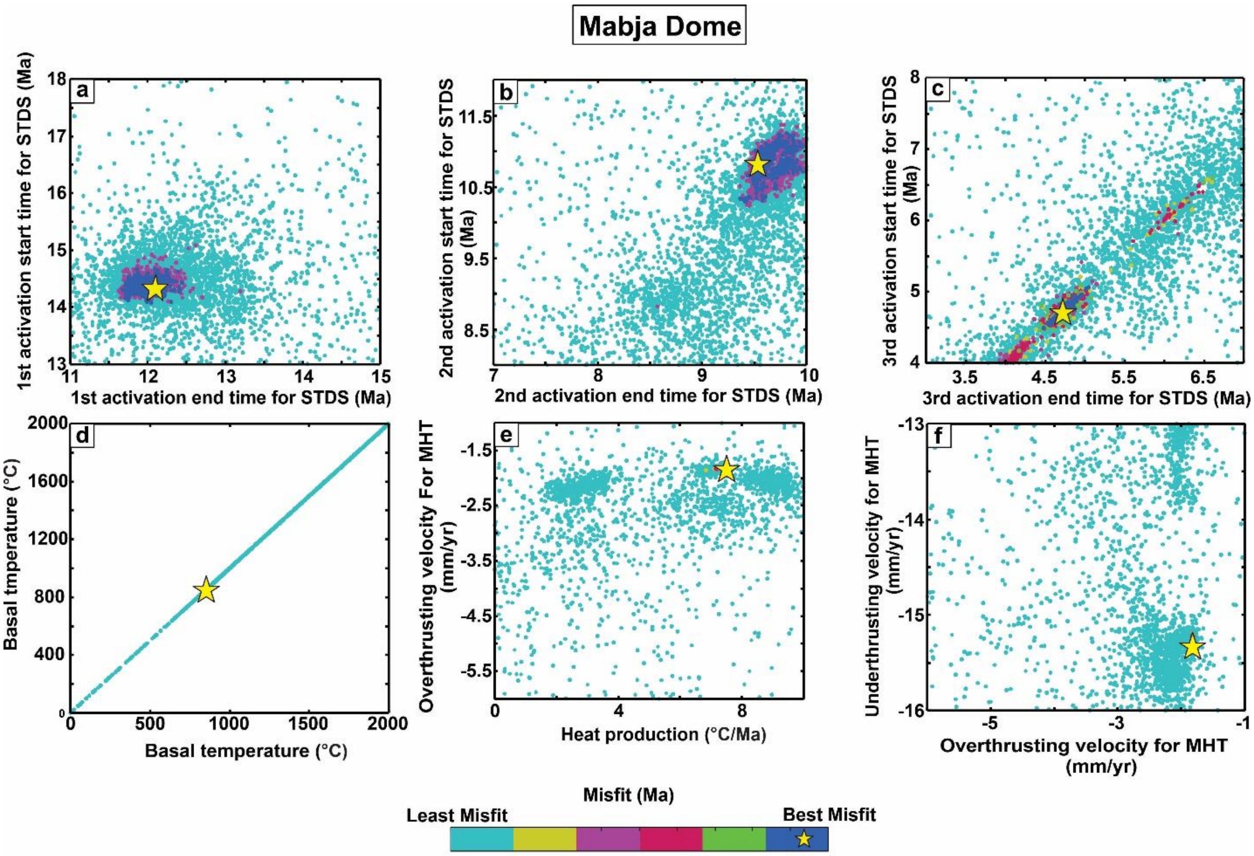

Fig. S19

Fig. S19: Figures a-f show the results of inverse model plots for different parameters for the Mabja Dome, where the yellow star mark represents the best fit.

2.3.6 Kampa Dome

A 3D model for Kampa Dome is simulated using a basal thickness of 57 km, and dimensions of nx is 4940, and ny is 11838 for the two-time scenario from 16 to 0 Ma, with all parameters given in Supplementary Table S3. In this model, we did not incorporate the age elevation relation, isostasy, or shear heating, and in contrast, three fault data obtained (Acton et al., 2011; Mitra et al., 2005; Lee et al., 2000; Grujic et al., 2011; Warren et al., 2011; Zhao et al., 1993) and employed to simulate the model by incorporating two types of thermochronological ages: MAr and BAr ages, while the model mainly used three faults, MHT, MCT and STDS, where MHT was considered as a thrust fault that remained active from 16 Ma to present, and STDS was modeled as a normal fault between 15 to 14 Ma, and MCT was modeled as a thrust fault between the 21 to 20 Ma. To determine the precise activation time in the brittle stage, the parameters were set within a range after seeing the predicted ages in the forward model. To determine the activation time in the brittle stage, predicted AFT and ZFT ages given by Pecube were used, while the forward model has the best RMS misfit result of 1.133 Ma. After forward modeling (supplementary Fig. S20, S21a-c), we did the inverse modeling using the neighborhood algorithm using Pecube, which has ranges and best fits, as given in supplementary Table S4 and inverse result displayed in Supplementary Fig. S22 (a-d).

The table below shows the number of model scenario tests to constrain the best RMS misfit.

Dome Names	Faults	Fault Parameters Used	RMS Misfit (Ma)	RMS Total Misfit (Ma)
Kampa Dome	Model Scenario 1 (Without MCT)	MHT (17Ma-0Ma) STDS (15 Ma-14 Ma)	MAr = 0.605 BAr = 1.238	1.133 **Most Viable Model**
	Model Scenario 2	MHT (17Ma-0Ma) STDS (15 Ma-14 Ma) MCT (21-20 Ma)	MAr = 2.025 BAr = 1.377	1.703
	Model Scenario 3 (Without MHT)	STDS (15 Ma-14 Ma, 6.5 Ma – 6 Ma) MCT (21-20 Ma)	MAr = 2.406 BAr = 1.401	1.721

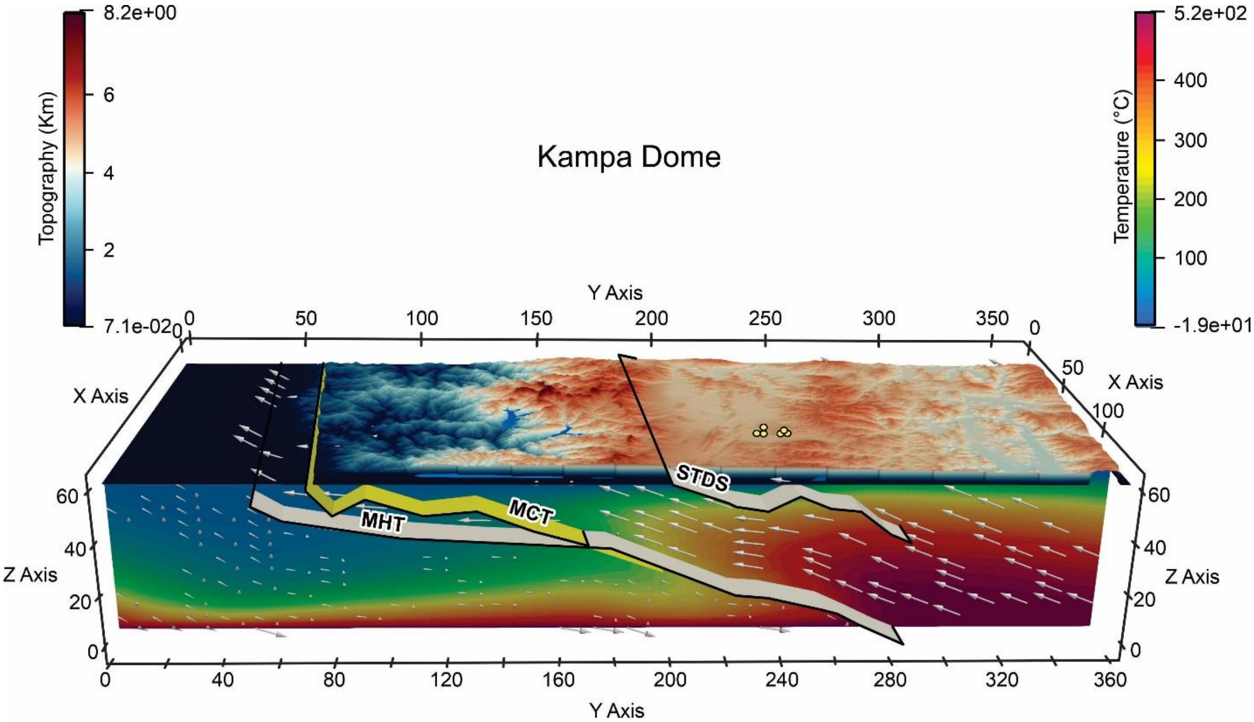

Fig. S20

Fig. S20: The Figure shows the 3D model for the Kampa Dome, where isotherms and velocity vectors demonstrated in the cross-sections are constrained after employing the Pecube Forward model.

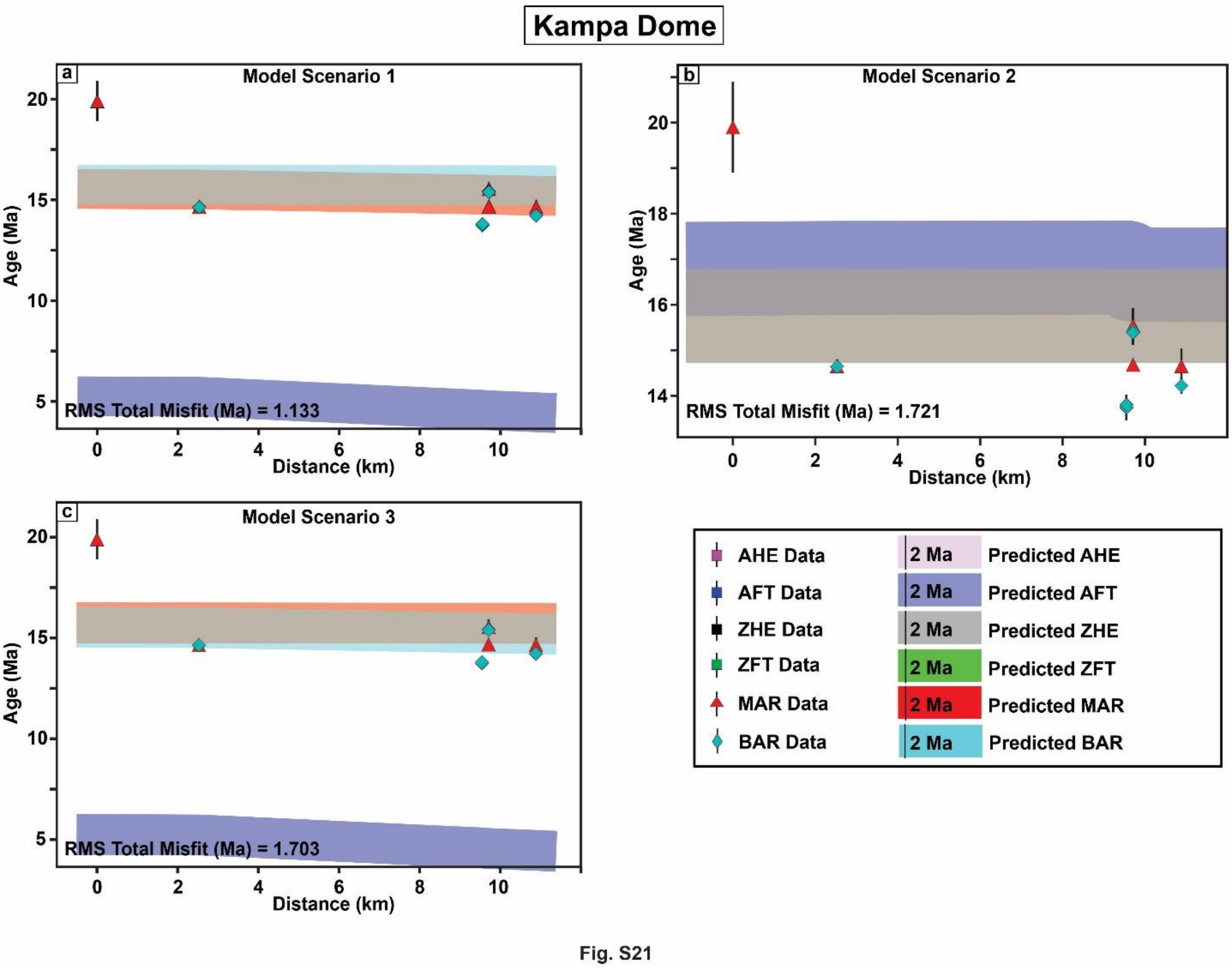

Fig. S21: Figures a-c illustrates the age distance plot for the observed and predicted for Kampa Dome in the Himalaya after Pecube forward models.

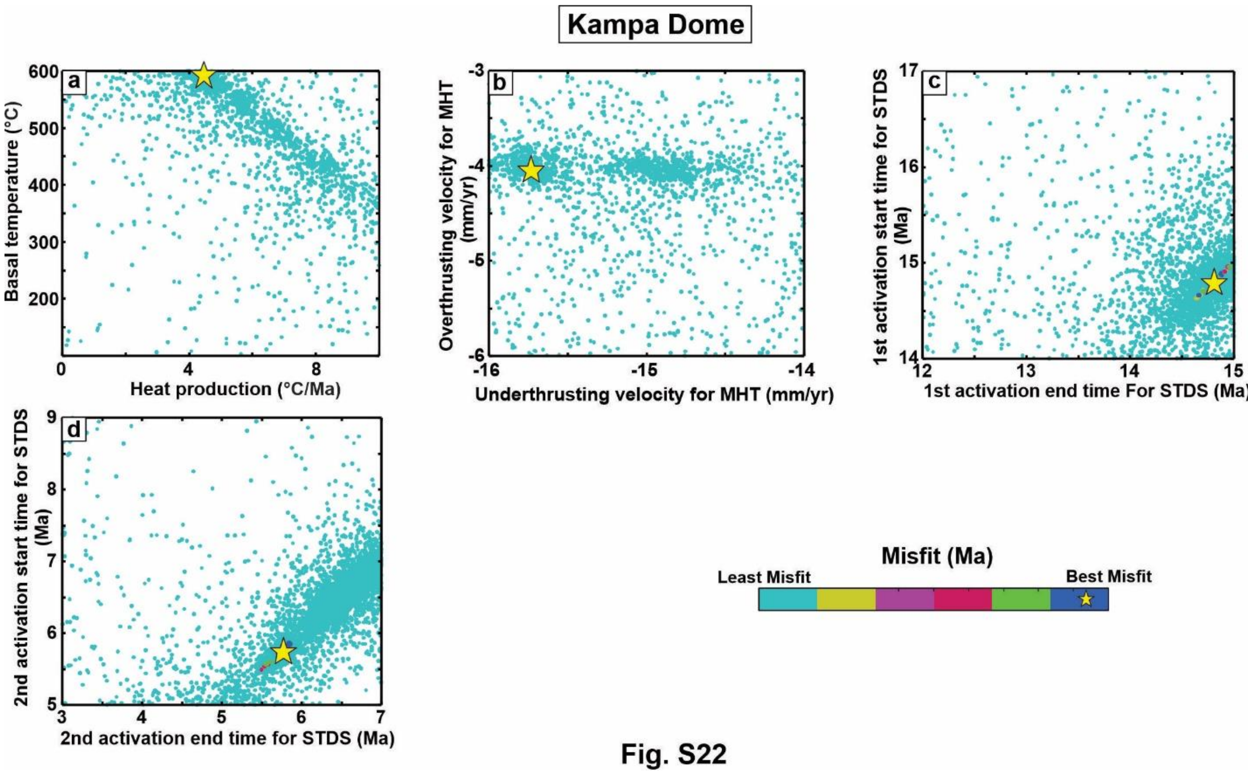

Fig. S22: Figures a-d show the results of inverse model plots for different parameters for the Kampa Dome, where the yellow star mark represents the best fit.

2.3.7 Kamgmar Dome

The 3D model of Kangmar domes was created using the 57 km Basal thickness and consists of dimensions having nx is 2481 and ny 11528, where a two-time tectonomorphic situation was taken for the modeling of this dome from 17.4 to 0 Ma. Where, we used the five thermochronological data known as MAr, BAr, AFT, ZFT, and ZHe ages. In contrast, age elevation, shear heating, and isostasy were not taken for the model, and three faults were used, obtained from Acton et al., 2011; Mitra et al., 2005; Lee et al., 2000; Grujic et al., 2011; Warren et al., 2011 and Zhao et al., 1993. Among these three faults, one is the MHT modeled as a thrust fault active from 17.4 to the present day, another fault is the STDS modeled as a normal fault active in two-time steps, where the first step was from 12.35 to 12.34 Ma, and the second step was taken from 7.3 to 3 Ma, while MCT modeled as a thrust fault active from 21-20 Ma. As a result, the model comprising the best RMS misfit is 2.544 Ma, and all those remaining parameters are discussed in the supplementary table S3. After forward modeling (supplementary Fig. S23, S24), we did the inverse modeling using the neighborhood algorithm using Pecube, which has ranges and best fits, as given in supplementary Table S4, and the inverse result is displayed in supplementary Fig. S25.

The table below shows the number of model scenario tests to constrain the best RMS misfit.

Dome Names	Faults	Fault Parameters Used	RMS Misfit (Ma)	RMS Total Misfit (Ma)
Kangmar Dome	Model Scenario 1 (Without MCT)	MHT (17.4 Ma-0 Ma) STDS (12.35 Ma-12.34 Ma, 7.3 Ma – 3 Ma)	AFT = 2.313 ZHe = 1.674 ZFT = 2.275 MAr = 1.997 BAr = 3.591	2.544 **Most Viable Model**
	Model Scenario 2	MHT (17.4 Ma-0 Ma) STDS (12.35 Ma-12.34 Ma, 7.3 Ma – 3 Ma) MCT (21-20 Ma)	AFT = 2.313 ZHe = 1.705 ZFT = 1.674 MAr = 2.08 BAr = 3.616	2.561
	Model Scenario 3 (STDS active one time)	MHT (17.4 Ma-0 Ma) STDS (12.35 Ma-12.34 Ma) MCT (21-20 Ma)	AFT = 2.946 ZHe = 4.839 ZFT = 8.101 MAr = 2.359 BAr = 2.909	3.975
	Model Scenario 4 (Without MHT)	STDS (12.35 Ma-12.34 Ma, 7.3 Ma – 3 Ma) MCT (21-20 Ma)	AFT = 1.535 ZHe = 7.297 ZFT = 2.017 MAr = 3.214 BAr = 3.777	3.54

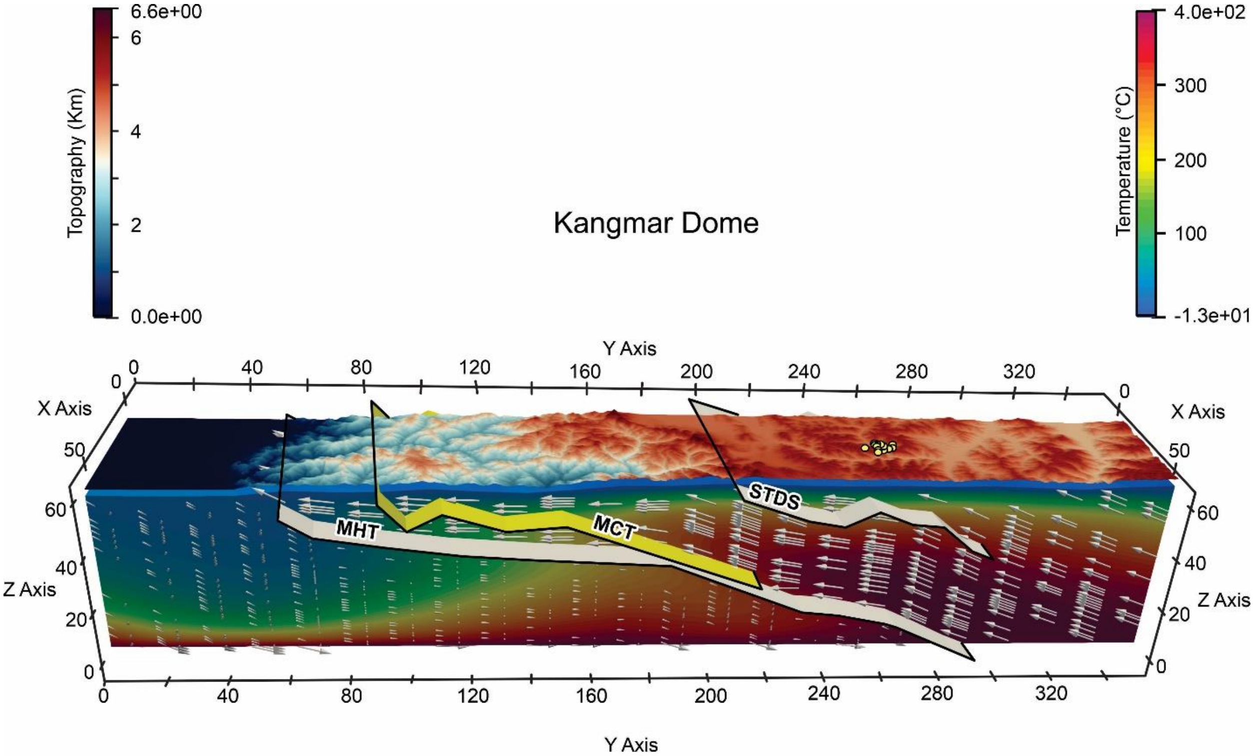

Fig. S23

Fig. S23: The Figure shows the 3D model for the Kangmar Dome, where isotherms and velocity vectors demonstrated in the cross-sections are constrained after employing the Pecube Forward model.

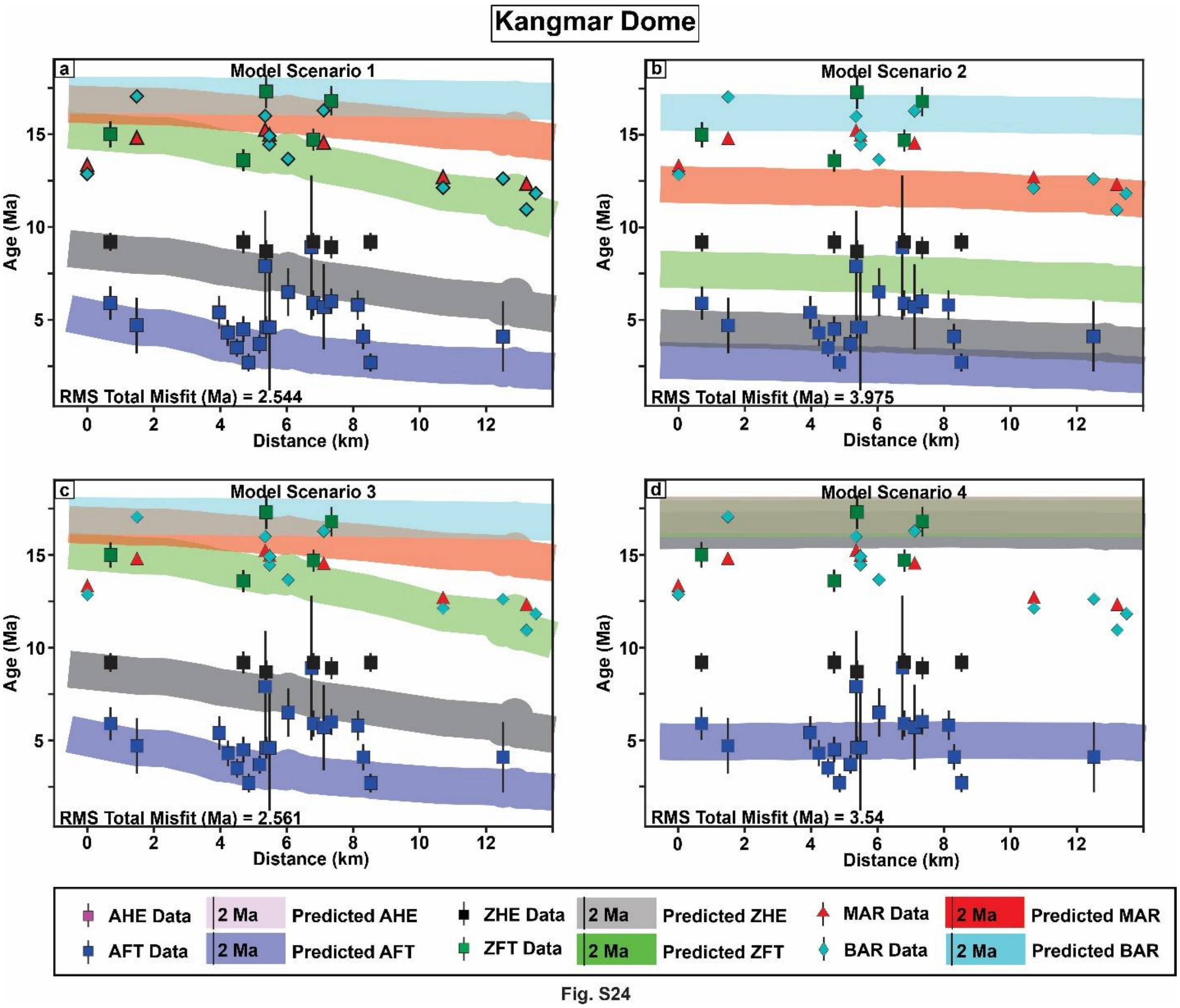

Fig. S24: Figures a-d illustrate the age distance plot for the observed and predicted for Kangmar Dome in the Himalaya after Pecube forward models.

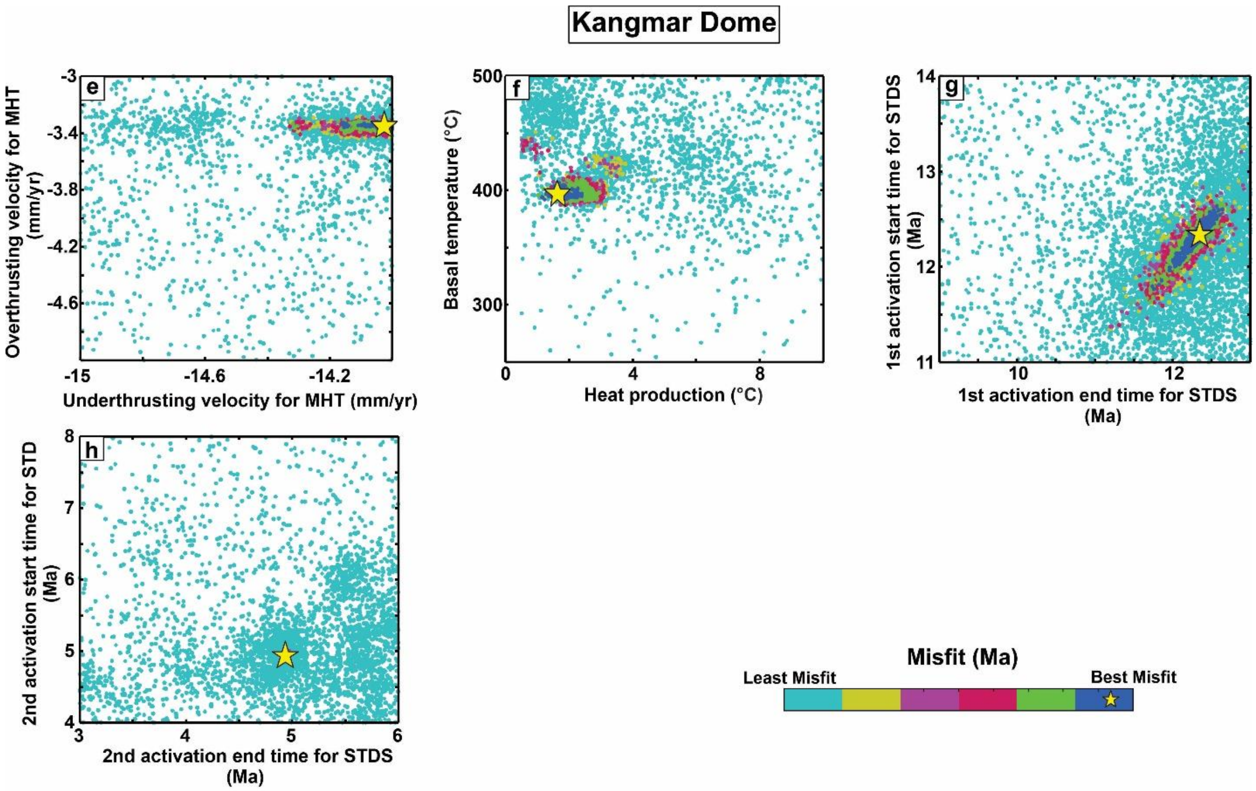

Fig. S25

Fig. S25: Figures a-h show the results of inverse model plots for different parameters for the Kangmar Dome, where the yellow star mark represents the best fit.

3. Normalized Channel Steepness Index (Ksn)

The normalized channel steepness index (Ksn) represents the ratio of the stream channel gradient to the drainage area (Kirby & Whipple, 2012), expressed by the formula:

$$S=k_{sn}A^{-\theta}$$

Where S is the channel slope, A is the drainage area in upstream, Ksn is the normalized channel steepness, and θ is the concavity index (Hack, 1957), whereas the θ is the ratio of two constant m and n depends on the hydrology of the basin, incision process and geometry of the channel (Mudd et al., 2018). We did the Ksn analysis within the gneissic doming region that is situated in the lithologically similar area on a regional scale by using normal θ is 0.45 (Clubb et al., 2023) to examine the fluvial response to tectonic forcing because the rapid tectonic uplift causes rapid stream incision. The methodology employed the SRTM 30m digital elevation model (DEM: https://opentopography.org/) and utilized LSDTopoTool (Mudd et al., 2014). The Ksn values of the gneissic domes (See Supply Fig. S26) of the Himalaya are demonstrated below:

Dome Name	**Ksn Values Range**
Gianbul Dome	0-501
Chisoti Dome	0-562
Suru Dome	0-400
LeoPargil Dome	0-522
Changgo Dome	0-2700
North Himalayan Gneissic Dome (Kangmar Dome, Kampa Dome, Mabja Dome)	0-382

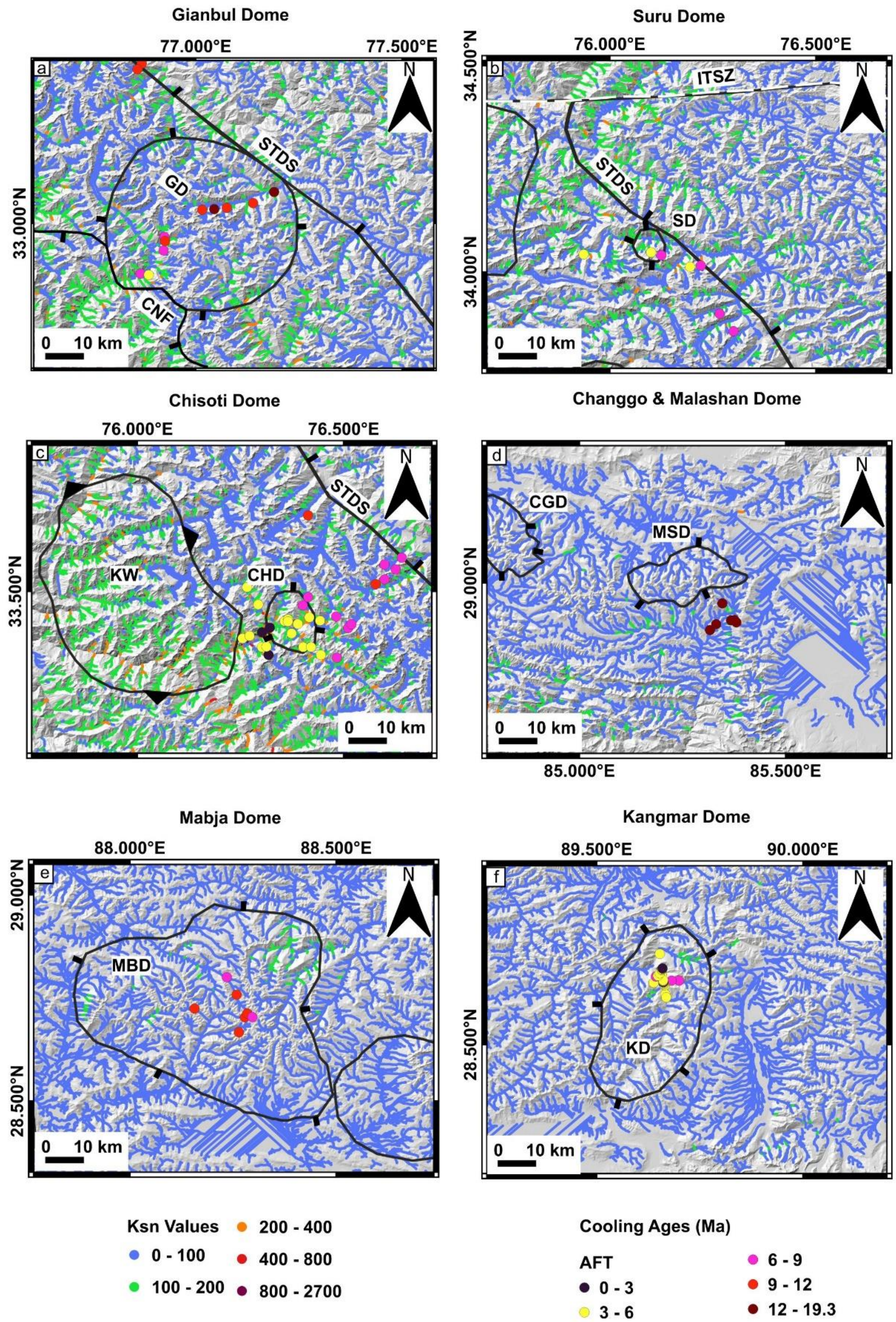
Gianbul Dome
77.000°E
77.500°E
a
N
STDS
GD
33.000°N
CNF
0 10 km
Suru Dome
76.000°E
76.500°E
34.500°N
b
ITSZ
STDS
SD
34.000°N
0 10 km
Chisoti Dome
76.000°E
76.500°E
c
STDS
KW
CHD
33.500°N
0 10 km
Changgo & Malashan Dome
d
CGD
MSD
29.000°N
0 10 km
85.000°E
85.500°E
Mabja Dome
88.000°E
88.500°E
29.000°N
e
MBD
28.500°N
0 10 km
Kangmar Dome
89.500°E
90.000°E
f
KD
28.500°N
0 10 km
Ksn Values
0 - 100
100 - 200
200 - 400
400 - 800
800 - 2700
Cooling Ages (Ma)
AFT
0 - 3
3 - 6
6 - 9
9 - 12
12 - 19.3

Fig. S26

Fig. S26: Figures a-f show the Ksn results with the youngest colling ages for the different gneissic domes of the Himalaya, where (a) Gianbul Dome, (b) Suru Dome, (c) Chisoti Dome, (d) Chaggo-Malashan Dome, (e) Mabja Dome, (f) Kangmar Dome.

4. Gravity Disturbance

Gravity disturbance is solely a gravitational phenomenon that represents the difference between observed and referenced gravity (Oliveira et al., 2018).

$$\delta gP = gP - \gamma P$$

In this equation, δg signifies the gravity disturbance, g refers to the measured gravity, γ indicates the normal gravity, and p denotes the specific observation point where the gravity measurement occurs. The measured gravity g is characterized as the magnitude of the gravitational acceleration, which is the spatial derivative of Earth's gravitational potential W, encompassing both the gravitational potential V (resulting from the attraction of Earth's mass) and the centrifugal potential Φ attributable to Earth's rotation.

$$W = V + \Phi$$

The normal gravity γ is described as the derivative of the potential gravity field produced by the reference ellipsoid U, which is the cumulative effect of the gravitational field *Vell* and the centrifugal potential Φ:

$$V = Vell + \Phi$$

Gravity disturbance is primarily utilized to identify geodynamic structures and to make inferences about the Earth's internal structure (Hofmann-WellenhofMoritz, 2006). The gravity disturbance

(Eigen-6C4) (https://icgem.gfz-potsdam.de/home) for the Himalaya is demonstrated in supplementary Fig. S27.

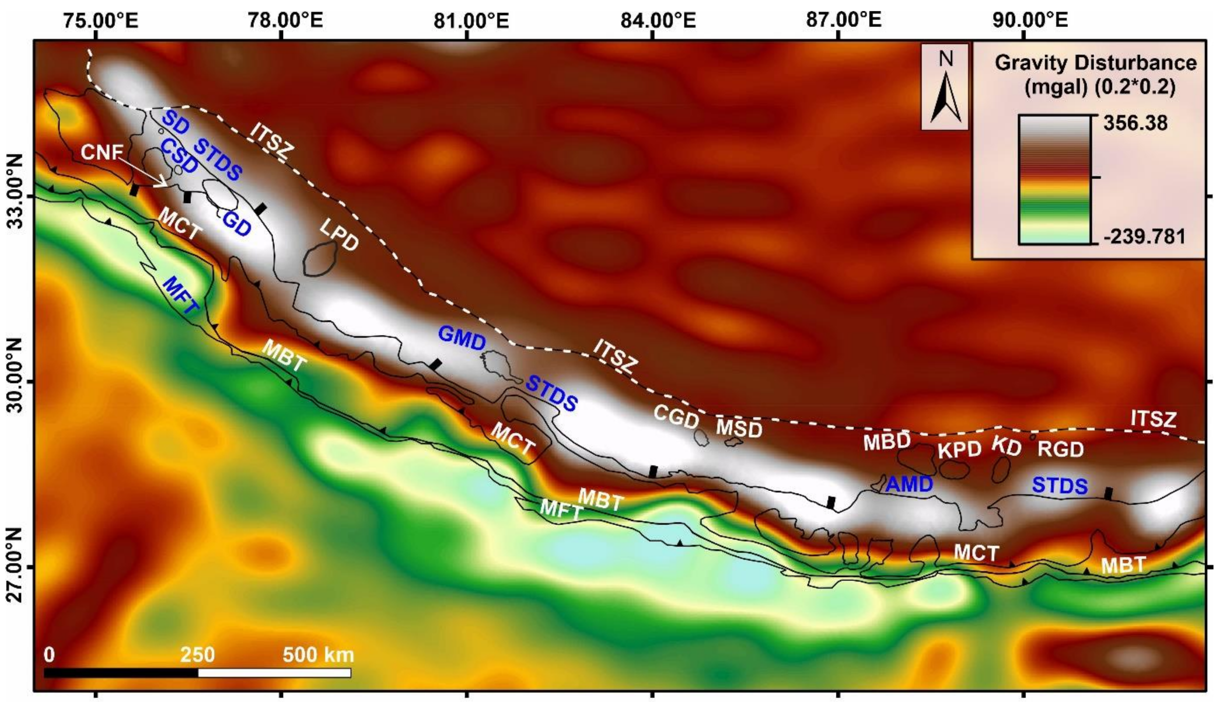

Fig. S27

Fig. S27: Gravity disturbance map of the Himalaya with location of the gneissic dome illustrates the gravity disturbed area.

Table S1a: Compiled cooling ages from different gneissic dome in the Himalaya.

Sl No.	Sample No.	Longitude	Lattitude	Elevation (m)	AHE	DAHE	AFT	DAFT	ZHE	DZHE	ZFT	DZFT	MAR	DMAR	BAR	DBAR	References and Domes Name
1.	GBD-5c	76.90175	32.93034	3882									20.7	0.1	21.3	0.2	Gianbul Dome Horton et al., 2015 And This Study
2.	GBD-15	76.90836	32.94436	4084									20.7	0.2			
3.	GBD-26c	76.88536	32.95797	4109									20.7	0.1	21.4	0.2	
4.	GBD-29b	76.88853	32.96137	4263									20.7	0.2			
5.	GBD-33	76.91902	32.98282	4292											22	0.2	
6.	GBD-34	76.9197	32.9813	4283											23	0.2	
7.	GBD-36b	76.91834	32.9747	4379									20.8	0.1	22.6	0.2	
8.	GBD-38	76.91959	32.96735	4322									21.1	0.2			
9.	GBD-45b	76.89998	32.90104	3832											21.8	0.1	
10.	GBD- 51b	76.83001	32.86728	3471											25.9	0.2	
11.	GBD-52b	76.83075	32.8673	3466									21.4	0.1	25.1	0.2	
12.	GBD-57a	77.15437	33.07651	4321									20.2	0.2	20.4	0.1	
13.	GBD-60b	77.15351	33.07519	4281									21.4	0.3	21.4	0.1	
14.	GBD- 63b	77.11447	33.05773	4373									19.7	0.1	19.8	0.1	
15.	GBD-64c	77.11371	33.05815	4403									19.8	0.2	19.6	0.2	
16.	GBD- 64d	77.11371	33.05815	4399									20.1	0.2	19.9	0.2	
17.	GBD-67a	77.11839	33.05863	4379									19.9	0.2			
18.	GBD-79c	77.13253	33.06576	4370									20.4	0.2	22.7	0.2	
19.	GBD-90b	77.09758	33.05584	4436									20.2	0.2	21.6	0.2	
20.	GBD-100b	77.03239	33.04867	4484									21.1	0.2	20.9	0.2	
21.	GBD-101b	77.02861	33.04776	4491											22.5	0.1	
22.	GD-3	77.139	33.049	4642			9.9	0.8			15.4	0.7					

23.	GD-6	77.0156	33.0328	5128			12	0.6									
24.	GD-7	77.0447	33.0344	5005			14.2	1.2			22.8	2.2					
25.	GD-8	77.0752	33.0379	4799			11.7	0.7									
26.	GD-9	77.156	33.0595	4649							14.6	0.9					
27.	GD-10	77.17	33.068	4450							18.5	3.1					
28.	GD-11	77.19	33.076	4133			12.7	0.4									
29.	M1	76.924	32.967	4162			6.4	0.5			17.6	1.3					
30.	M2	76.9255	32.957	4090			10.7	0.7									
31.	M3	76.922	32.934	4911			8.2	0.4									
32.	K3	76.866	32.878	3575			7.9	0.6									
33.	KU1	76.886	32.875	4121			5.7	1.1			16.9	1.1					
34.	K1	76.898	33.883	4211							17	0.9					
35.	PIAP	76.7397	33.53132	4643			8.04	0.37									Suru Dome Kumar et al., 1995
36.	P3AP	76.64109	33.58173	4892			7.61	0.39									
37.	P4AP	76.59948	33.52893	5155			8.07	0.43									
38.	P5AP	76.5778	33.51756	4664			9.52	0.22									
39.	P6AP	76.62631	33.55361	5313			7.48	0.25									
40.	P7AP	76.85072	33.43211	4916			9.54	0.29									
41.	P8AP	76.8662	33.41501	5041			6.34	0.25									
42.	P9AP	76.86916	33.38745	5365			10.33	0.37									
43.	P1OAP	76.85867	33.37335	5568			9.71	0.24									
44.	P11AP	76.7419	33.46171	5653			9.66	0.27									
45.	P12AP	76.75115	33.47618	5061			11.04	0.28									
46.	P13AP	76.77932	33.49205	4588			11.67	0.64									
47.	P15AP	76.41393	33.68437	4772			10.79	0.59									
48.	P16AP1	76.26662	33.89859	4910			8.12	0.41									
49.	P16AP2	76.26662	33.89859	4910			7.64	0.59									
50.	P17AP	76.30023	33.85618	5605			7.65	0.43									
51.	P18AP	76.22101	34.01541	4698			7.33	0.99									
52.	P19AP	76.10019	34.04741	5538			4.93	0.31									
53.	P20AP	76.1252	34.0403	4623			6.36	0.34									

54.	P21AP	75.93675	34.04259	3839			5.57	0.55									
55.	P23AP	76.72135	33.54312	4407			10.26	0.3									
56.	P25AP	76.19501	34.01244	5614			5.32	0.29									
57.	P6ZR	76.626	33.553	5304							12.52	1.33					
58.	H19	76.0098	34.083	3600											15.15	0.34	
59.	H24	76.179	34.059	4120											19.97	0.45	
60.	H33	76.378	33.970	4280											22.55	0.50	
61.	P18/74	76.599	33.565	4140			8.1	0.4							24.9	0.6	Chisoti Dome Sorkhabi et al., 1996
62.	P49/189	76.741	33.503	4080			11	0.3							19.7	0.4	
63.	U21/21	76.482	33.439	4440			7.1	0.3							17.4	0.4	
64.	U32/34	76.417	33.437	3420			4.9	0.4							16.8	0.4	
65.	U50/53	76.402	33.365	3360			5.5	0.2							15.8	0.4	
66.	U77/89	76.255	33.386	2360			4.4	0.5							13.7	0.3	
67.	A63/77	76.357	33.428	2800			4.1	0.2							16.1	0.4	
68.	A67/87	76.365	33.432	3480			4.9	0.3							17.4	0.4	
69.	KUM1	76.266	33.51	3653			4.1	0.2			10	0.6					Chisoti Dome Kumar et al., 1995
70.	KUM2	76.293	33.468	3462			3.6	0.5									
71.	KUM3	76.414	33.486	3967			6.5	0.4			10.8	0.8					
72.	KUM4	76.401	33.466	4369			6.3	0.2									
73.	KUM5	76.443	33.429	3844			4.9	0.4									
74.	KUM6	76.511	33.411	4352			7.1	0.3									
75.	KUM7	76.5192	33.4203	4470			8	0.3			12.3	0.7					
76.	KUM8	76.484	33.339	4656			7.1	0.3									
77.	KUM9	76.445	33.346	3912			5.2	0.3									
78.	KUM10	76.421	33.365	3628			5.5	0.2									
79.	KUM11	76.389	33.421	3447			4.9	0.3									
80.	KUM12	76.374	33.398	3301			4.5	0.4									
81.	KUM13	76.365	33.427	3887			4.1	0.2			6.5	0.6					
82.	KUM14	76.321	33.412	3043			3	0.2									
83.	KUM15	76.318	33.346	4946			2.6	0.3									
84.	KUM16	76.302	33.365	3884			5	0.5									
85.	KUM17	76.313	33.366	4535			4.2	0.4			8.4	0.7					
86.	KUM18	76.3022	33.4008	3239			2.1	0.2			6.8	0.4					
87.	KUM19	76.272	33.392	3113			4.4	0.5			6.2	0.6					
88.	Â KT202	84.8238	29.1784	4975									21.29	0.16			
89.	Â CH122 B	84.8163	29.135	5724									18.43	0.25			

90.	Â CH123 B	84.8117	29.1301	5393									17.62	0.25	16.76	0.22	Changgo-Malashan Dome Larson et al., 2010
91.	Â KTG9A	84.7847	29.1446	5491									18.82	0.08			
92.	Â KTG9C	84.7847	29.1446	5491									18.65	0.06			
93.	Malashan	85.251	29.007	5570									15.93	0.04	15.5	0.06	Aoya et al., 2006
94.	Aoya1	85.4398	29.0047	4807									15.93	0.04	15.50	0.06	Aoya et al., 2005
95.	Aoya2	85.3468	28.9652	5809									15.68	0.03	15.27	0.06	
96.	Shen1	85.3167	28.8857	4286			16	1.5									Shen et al., 2016
97.	Shen2	85.3317	28.9	4337			15.8	1.5									
98.	Shen3	85.3678	28.9092	4936			13.4	0.95									
99.	Shen4	85.3761	28.9101	5016			16.6	1.25									
100.	Shen5	85.3808	28.9043	5157			19.3	1.75									
101.	Shen6	85.3467	28.9505	5156			17.2	1.1									
102.	GD05	88.563	28.487	4960													Kampa Dome Quigley et al., 2006
103.	GDO8b	88.628	28.4724	4612											14.64	0.15	
104.	GD08m	88.628	28.4724	4612									14.65	0.08			
105.	GD12	88.609	28.457	4598									19.9	1			
106.	GD23b	88.624	28.554	4715											14.22	0.18	
107.	GD23m	88.624	28.554	4715									14.65	0.39			
108.	GD25	88.623	28.542	4690											13.74	0.28	
109.	GD26	88.623	28.542	4690											13.8	0.07	
110.	GD28b	88.62	28.5438	4681											15.42	0.3	
111.	GD28m	88.62	28.5438	4681									14.68	0.07			
112.	GD30b	88.62	28.5438	4681											15.39	0.23	
113.	GD30m	88.62	28.5438	4681									15.54	0.39			
114.	KD09C	89.66667	28.62167	4300									14.82	0.04			Kangmar Dome Lee et al., 2000
115.	KD12C	89.65667	28.72667	4200									12.33	0.03	10.94	0.03	
116.	KD13B	89.65333	28.72	4170			4.1	1.9							12.61	0.03	
117.	KD20	89.65833	28.67167	4250			5.7	2.3					14.56	0.05	16.28	0.04	
118.	KD42AA	89.7	28.655	4700			6.5	1.3							13.66	0.03	
119.	KD56AA	89.63833	28.65	4560			4.6	3.4							14.46	0.03	
120.	KD56BB	89.63833	28.65	4560									14.98	0.03	14.91	0.03	
121.	KD61	89.68167	28.655	4480			7.9	3					15.24	0.05	15.99	0.04	
122.	KD77	89.64833	28.72833	4230											11.82	0.03	

123.	KD87B	89.66833	28.60833	4340									13.35	0.03	12.86	0.04	
124.	KD88B	89.66667	28.62167	4300			4.7	1.5					14.82	0.03	17.04	0.04	
125.	KD89	89.635	28.7	4470									12.71	0.04	12.12	0.03	
126.	D0812	89.6688	28.6146	5100			5.9	0.9	9.2	0.5	15	0.7					Ma et al., 2023
127.	D0813	89.6653	28.6439	5000			5.4	0.9									
128.	D0814	89.6631	28.6461	4900			4.3	0.7									
129.	D0815	89.6624	28.6485	4800			3.5	0.5									
130.	D0816	89.6623	28.6502	4700			4.5	0.7	9.2	0.6	13.6	0.6					
131.	D0817	89.6618	28.6516	4620			2.7	0.5									
132.	D0819	89.6613	28.6545	4460			3.7	0.5									
133.	D0820	89.6614	28.6563	4380			4.6	0.6	8.7	0.6	17.3	0.9					
134.	D7101	89.6437	28.665	5060			8.9	3.9									
135.	D7103	89.6486	28.667	4860			5.9	0.7	9.2	0.5	14.7	0.6					
136.	D7105	89.6531	28.673	4660			6	0.7	8.9	0.6	16.8	0.8					
137.	D7107	89.6577	28.6809	4420			5.8	0.8									
138.	D7108	89.6587	28.6825	4310			4.1	0.7									
139.	D7109	89.6597	28.6846	4200			2.7	0.5	9.2	0.5							
140.	MD31B	88.2239	28.80598	4921									12.79	0.12			Mabja Dome Lee et al., 2006
141.	MD48A	88.2786	28.72873	5484									14.03	0.14	15.37	0.14	
142.	MD52	88.27867	28.70325	5588			9.5	1.2					13.39	0.12	13.6	0.12	
143.	MD79	88.202	28.6924	5095									16.77	0.15	15.88	0.15	
144.	MD86	88.15667	28.7243	5328			9.2	1.2					13.14	0.05	12.93	0.06	
145.	MD97	88.26438	28.66685	5378			9.9	2.3					13.54	0.05			
146.	MD100	88.2327	28.7095	5234									16.27	0.15			
147.	MD47	88.2022	28.69386	5058									16.99	0.15			
148.	MD49A	88.25995	28.74848	5213									15.37	0.14			
149.	MD71	88.28447	28.71259	5628			11.5	1.6					13.48	0.12	13.6	0.11	
150.	MD64A	88.29698	28.70365	5557			8.4	1.4					13.69	0.12	13.79	0.13	
151.	MD69B	88.3046	28.6979	5627									13.33	0.06			
152.	MD33	88.23515	28.80046	5069			8.3	2.3							15.51	0.14	
153.	MD39	88.2589	28.7579	5284			10.7	2.6							17.6	0.15	
154.	MD37	88.28096	28.71422	5518											13.49	0.12	
155.	MD69A	88.2856	28.71486	5472											13.48	0.11	

Table S1b: Compiled cooling ages from MCT to STDS in the NW Himalaya.

SAMPLE	LON	LAT	HEIGHT	AHE	DAHE	AFT	DAFT	ZHE	DZHE	BAR	DBAR	MAR	DMAR	References
GBD-5c	76.90175	32.93034	3882							21.3	0.2	20.7	0.1	Horton et al., 2014
GBD-15	76.90836	32.94436	4084									20.7	0.2	
GBD-26c	76.88536	32.95797	4109							21.4	0.2	20.7	0.1	
GBD-29b	76.88853	32.96137	4263									20.7	0.2	
GBD-33	76.91902	32.98282	4292							22	0.2			
GBD-34	76.9197	32.9813	4283							23	0.2			
GBD-36b	76.91834	32.9747	4379							22.6	0.2	20.8	0.1	
GBD-38	76.91959	32.96735	4322									21.1	0.2	
GBD-45b	76.89998	32.90104	3832							21.8	0.1			
GBD- 51b	76.83001	32.86728	3471							25.9	0.2			
GBD-52b	76.83075	32.8673	3466							25.1	0.2	21.4	0.1	
GBD-57a	77.15437	33.07651	4321							20.4	0.1	20.2	0.2	
GBD-60b	77.15351	33.07519	4281							21.4	0.1	21.4	0.3	
GBD- 63b	77.11447	33.05773	4373							19.8	0.1	19.7	0.1	
GBD-64c	77.11371	33.05815	4403							19.6	0.2	19.8	0.2	
GBD- 64d	77.11371	33.05815	4399							19.9	0.2	20.1	0.2	
GBD-67a	77.11839	33.05863	4379									19.9	0.2	
GBD-79c	77.13253	33.06576	4370							22.7	0.2	20.4	0.2	
GBD-90b	77.09758	33.05584	4436							21.6	0.2	20.2	0.2	
GBD-100b	77.03239	33.04867	4484							20.9	0.2	21.1	0.2	
GBD-101b	77.02861	33.04776	4491							22.5	0.1			
AD07-01	76.8679	32.6065	3105			4.3	0.5	12.6	1.3					Deeken et al., 2011
AD07-02	76.8532	32.59	3380			5.3	0.6	14.9	1.5					
AD07-03	76.8536	32.5759	3625			3.5	0.8	14.1	1.4					
AD07-04	76.8475	32.5585	4030			5	0.7	13.6	1.4					
AD07-05	76.8371	32.5351	4615			6.3	1	17	1.7					
AD07-06	76.8313	32.5291	5070			6.7	0.9	15.1	1.5					
AD07-07	76.808	32.5131	3900			9.3	0.9	18.1	1.8					
AD07-08	76.7899	32.4993	3715			5.4	0.7	15.5	1.6					
AD07-09	76.7713	32.4997	3455			3.8	0.7							
AD07-10	76.6917	32.4717	2515			2	0.5							
AD07-12	76.4509	32.4666	1465			2.3	0.4	11.8	1.2					
AD07-13	76.53	32.3502	1730			1.7	0.3							
AD07-14	76.4666	32.353	2055					9.4	1.3					
AD07-15	76.4114	32.3288	2985			2.8	0.4							
AD07-16	76.3933	32.306	3705			2.8	0.4	11.2	1.1					
AD07-17	76.9812	32.297	4340			2.4	0.5	12.2	1.2					
AD07-18	76.3836	32.2992	4230			3.7	0.4	14.5	1.5					
AD07-19	76.3735	32.2899	3620					9.2	0.9					
AD07-20	76.3694	32.2853	3300			3.2	0.5	8.3	0.8					
AD07-22	76.3584	32.278	3130			2.9	0.2	6.4	0.6					

AD07-23	76.3441	32.325	2460	2.8	0.3	6.3	0.6
AD07-28	76.038	32.4573	1980	4.4	0.3		
AD07-29	76.0556	32.4885	2405			13	0.6
AD07-42	76.37	32.0848	2305			7.4	0.7
AD07-43	77.118	32.806	4080	7.1	0.5	14	1.4
AD07-47	77.175	32.696	3515	5.9	0.5	13.5	1.4
AD07-49	76.8228	32.8647	3360	5.9	0.7	13.8	1.4
AD07-50	76.8742	32.8729	3705			12.6	1.3
AD07-51	76.7842	33.0559	4270			11.4	1.1
AD07-52	76.7925	33.0555	4600	8.7	0.5	12.3	1.2
AD07-53	76.8314	32.9921	4170	7.7	0.5	13.3	1.3
AD07-54	76.8168	32.987	4570	7.4	0.5	15.3	1.5
AD07-55	76.8094	32.9907	5050			13.8	1.4
AD07-56	76.8094	32.9907	5050	6.39	1		
AD07-57	76.76385	32.8417	2930	4.8	0.5	11.8	1.2
AD07-58	76.6696	32.7277	2645			16.3	1.6

Table. S2: Apatite and Zircon fission track results from Gianbul Dome.

Sl. No	Sample code	Longitude (E)	Latitude (N)	Ele. (m)	Lithology	No of Grains	Spontaneous track density Ns ρs × 10^6 cm^{-2}		Induced track density Ni ρi × 10^6 cm^{-2}		Glass dosimeter Nd ρd × 10^6 cm^{-2}		P (χ^2)%	U (ppm)	Central age ± 1σ (Ma)
1	GD3 A	77.139	33.049	4642	Migmatite	16	226	0.139	4977	3.012	3866	1.683	19.79	26.8	9.9 ± 0.8
2	GD3 Z	77.139	33.049	4642		18	1502	5.871	2504	9.650	2427	0.485	11.36	994	15.4 ± 0.7
3	GD6 A	77.0156	33.0328	5128	Migmatite	29	535	0.148	9675	2.724	3866	1.683	25.63	24.3	12 ± 0.6
4	GD7 A	77.0447	33.0344	5005	Migmatite	21	237	0.223	3685	3.297	3866	1.683	6.84	29.4	14.2 ± 1.2
5	GD7 Z	77.0447	33.0344	5005		12	222	2.814	245	3.310	2427	0.485	97.51	340	22.8 ± 2.2
6	GD8 A	77.0752	33.0379	4799	Migmatite	25	338	0.128	6300	2.391	3866	1.683	18.47	21.3	11.7 ± 0.7
7	GD9 Z	77.156	33.0595	4649	Kyanite Schist	8	414	3.248	722	5.191	2427	0.485	50.41	534.7	14.6 ± 0.9
8	GD10 Z	77.17	33.068	4450	Garnet Schist	13	112	2.567	198	4.228	2427	0.485	12.22	435.5	18.5 ± 3.1
9	GD11 A	77.19	33.076	4133	Phyllite	20	944	0.555	16555	9.806	8663.5	1.733	87.27	84.9	12.7 ± 0.4
10	K1 Z	76.898	32.883	4211	Orthogneiss	12	819	3.721	1215	5.596	2427	0.485	20.81	576.5	17 ± 0.9
11	K3 A	76.866	32.878	3575	Orthogneiss	27	256	0.113	7209	3.226	8663.5	1.733	28.14	27.9	7. 9 ± 0.6
12	KU1 A	76.886	32.875	4121	Granite	9	26	0.03	987	1.144	3866	1.683	89.37	10.2	5.7 ± 1.1
13	KU1 Z	76.886	32.875	4121		14	470	5.705	708	8.772	2427	0.485	75.43	903.6	16.9 ± 1.1
14	M1 A	76.924	32.967	4162	Migmatite	23	299	0.202	10164	6.924	3866	1.683	5.21	61.7	6.4 ± 0.5
15	M1 Z	76.924	32.967	4162		11	352	6.604	508	9.880	2427	0.485	51.91	1017.7	17.6 ± 1.3
16	M2 A	76.9255	32.957	4090	Schist	25	315	0.63	6379	1.276	3866	1.683	27.8	113.7	10.7 ± 0.7
17	M3 A	76.922	32.934	4911	Schist	24	547	0.259	14908	7.159	8663.5	1.733	9.26	62	8.2 ± 0.4

Table. S3 Thermal and Mechanical Parameter Values Specific for Pecube Forward Modeling.

Parameters name	Value	Units	References
Crustal Density	2700	kg/m3	Valla et al. (2010)
Mantle Density	3200	kg/m3	Valla et al. (2010)
Young's modulus	1×10^{11}	Pa	Ge et al.(2020)
Poisson ratio	0.25		Ge et al.(2020)
Equivalent elastic thickness	28.8	km	Ge et al.(2020)
Model thickness			
Gianbul Dome	40	Km	Dezes et al., 1999
Suru Dome	35	Km	
Chisoti Dome	35	Km	
Changgo -Malashan Dome	60	Km	
Mabja Dome	35	Km	
Kampa Dome	57	Km	
Kangmar Dome	57	Km	
nx*ny			
Gianbul Dome	7952*6782	Km	
Suru Dome	10616*8564	Km	
Chisoti Dome	10616*8564	Km	
Changgo -Malashan Dome	6803*9512	Km	
Mabja Dome	4940*11838	Km	
Kampa Dome	4940*11838	Km	
Kangmar Dome	2481*11528	Km	
Thermal Diffusivity	25	km^2/Ma	Braun and Robert (2005)
Temperature at the base of the model	550	°C	
Gianbul Dome	400	°C	
Suru Dome	650	°C	
Chisoti Dome	550	°C	
Changgo -Malashan Dome	350	°C	
Mabja Dome	510	°C	

Kampa Dome Kangmar Dome	395	°C	
Temperature at sea level	20	°C	Thiede et al., 2017
Atmospheric Lapse Rate	6	°C/km	Adlakha et al., 2013 Naito et al., 2006 Thiede et al., 2017
Crustal heat production Gianbul Dome Suru Dome Chisoti Dome Changgo -Malashan Dome Mabja Dome Kampa Dome Kangmar Dome	 7.75 3.5 7.5 2.7 3.5 4.5 2.5	 °C Ma^{-1} °C Ma^{-1} °C Ma^{-1} °C Ma^{-1} °C Ma^{-1} °C Ma^{-1} °C Ma^{-1}	 Adlakha et al., 2013
Space in degrees of longitude and latitude	0.00027	°	SRTM 30 DEM

Table. S4 Thermal and Mechanical Parameter Values Specific for Pecube Inverse Modeling.

Domes Name	Parameters		Parameters Range for inverse modeling	No. of forward models run for taken parameters	Best fit after inverse modeling	NA Misfit
Gianbul Dome	Basal Temperature (°C)		500:1000	5794	749.799	2.03
	Heat production (°C/Ma)		7:10	5794	8.918	2.03
	CNF	1st activation start time (Ma)	18:26	17529	21.644	0.320
		1st activation end Time (Ma)	13:23	17529	19.065	0.320
		2nd activation start time (Ma)	2:8	23630	3.9603	0.41846
		2nd activation end time (Ma)	1:7	23630	3.8786	0.41846
	STDS	1st activation start time (Ma)	20.5:22	9458	21.707	0.308
		1st activation end Time (Ma)	19:20.5	9458	19.00	0.308
		2nd activation start time (Ma)	6:7	9458	6.792	0.308
		2nd activation end time (Ma)	5:6	9458	5.66	0.308
	MCT	1st activation start time (Ma)	18:26	34880	22.6556	0.41569
		1st activation end Time (Ma)	13:23	34880	21.4818	0.41569
		2nd Segment Depth from MSL (km)	-5:-9	12059	-5.17	1.08
		3rd Segment Depth from MSL (km)	-8:-15	12059	-14.86	1.08
		4th Segment Depth from MSL (km)	-15:-20	12059	-19.99	1.08
		5th Segment Depth from MSL (km)	-17:-21	12665	-19.24	1.10
		6th Segment Depth from MSL (km)	-17:-22	12665	-21.97	1.10
		7th Segment Depth from MSL (km)	-22:-26	12665	-25.98	1.10

	MHT	Overthrusting velocity (cm/yr)	0:-7	48268	-4.5795	0.42703
		Underthrusting velocity (cm/yr)	-1:-17	48268	-13.4341	0.42703
Suru Dome	Basal Temperature (°C)		500:1000	3144	500.11	0.22609
	Heat production (°C/Ma)		3:10	3144	4.263	0.22609
	STDS	1st activation start time (Ma)	20.5:23	11163	20.95	0.24827
		1st activation end Time (Ma)	19:20.5	11163	19.82	0.24827
		2nd activation start time (Ma)	6:8	23316	7.04	0.34815
		2nd activation end time (Ma)	3:5	23316	3.40	0.34815
	MCT	1st activation start time (Ma)	20.5:23	23316	21.95	0.34815
		1st activation end Time (Ma)	19:20.5	23316	19.71	0.34815
	MHT	Overthrusting velocity (cm/yr)	-4:-6	11163	-4.38	0.24827
		Unerthrusting velocity (cm/yr)	-14:-17	11163	-15.400	0.24827
Chisoti Dome	Basal Temperature (°C)		500:1000	10247	723.88	0.864
	Heat production (°C/Ma)		3:10	16696	3.00	0.971
	CNF	1st activation start time (Ma)	19.5:22	18433	19.82	1.275
		1st activation end Time (Ma)	18:19.5	18433	18.03	1.275
		2nd activation start time (Ma)	5:8	18433	6.14	1.275
		2nd activation end time (Ma)	3:5.5	18433	3.909	1.275
	STDS	1st activation start time (Ma)	20:22	10247	20.97	0.864
		1st activation end Time (Ma)	18:20	10247	19.27	0.864

		2nd activation start time (Ma)	6:8	10247	7.99	0.864
		2nd activation end time (Ma)	4:6	10247	4.54	0.864
	MCT	1st activation start time (Ma)	21:22	18097	21.01	2.26
		1st activation end Time (Ma)	19:20	18097	19.22	2.26
	MHT	Overthrusting velocity (cm/yr)	-2:-5	4154	-2.45	1.18
		Underthrusting velocity (cm/yr)	-14:-16	4154	-15.745	1.18
Changgo-Malashan Dome	Basal Temperature (°C)		300:1000	3674	688.135	0.14732
	Heat production (°C/Ma)		0:10	3647	4.39	0.14732
	STDS	2nd activation start time (Ma)	17:21	5660	18.911	0.30757
		2nd activation end time (Ma)	14:18	5660	17.518	0.30757
		2nd activation start time (Ma)	4:8	23769	4.2659	0.63259
		2nd activation end time (Ma)	3:7	23769	4.2283	0.63259
	MHT	Overthrusting velocity (cm/yr)	-3:-6	3674	-4.064	0.14732
		Underthrusting velocity (cm/yr)	-13:-16	3647	-14.364	0.14732
Mabja Dome	Basal Temperature (°C)		0:2000	7671	852.0915	0.68197
	Heat production (°C/Ma)		0:10	6220	7.489	0.57871
	STDS	1st activation start time (Ma)	13:18	8630	14.35	1.3127
		1st activation end Time (Ma)	11:15	8630	12.094	1.3127
		2nd activation start time (Ma)	8:12	8630	10.80	1.3127
		2nd activation end time (Ma)	7:10	8630	9.54	1.3127
		3rd activation start time (Ma)	4:8	6432	4.727	1.314

		3rd activation end time (Ma)	3:7	6432	4.722	1.314
	MHT	Overthrusting velocity (cm/yr)	-1:-6	6220	-1.827	0.57871
		Underthrusting velocity (cm/yr)	-13:-16	6220	-15.337	0.57871
Kampa Dome	Basal Temperature (°C)		100:600	16115	591.861	1.3702
	Heat production (°C/Ma)		0:10	16115	4.470	1.3702
	STDS	1st activation start time (Ma)	14:17	39738	14.81	2.5166
		1st activation end Time (Ma)	12:15	39738	14.80	2.5166
		2nd activation start time (Ma)	5:9	11635	5.77	2.8414
		2nd activation end time (Ma)	3:7	11635	5.76	2.8414
	MHT	Overthrusting Velocity (cm/yr)	-3:-6	16115	-4.04	1.3702
		Underthrusting Velocity (cm/yr)	-14:-16	16115	-15.73	1.3702
Kangmar Dome	Basal Temperature (°C)		250:500	4883	395.527	0.59809
	Heat production (°C/Ma)		0.5:10	4883	1.635	0.59809
	STDS	1st activation start time (Ma)	11:14	12436	12.343	0.77334
		1st activation end Time (Ma)	9:13	12436	12.35	0.77334
		2nd activation start time (Ma)	4:8	16564	4.96	0.83006
		2nd activation end time (Ma)	3:6	16564	4.93	0.83006
	MHT	Overthrusting velocity (cm/yr)	-3:-5	4883	-3.343	0.59809
		Underthrusting velocity	-14:-15	4883	-14.026	0.59809

References

Acton, C. E., Priestley, K., Mitra, S., & Gaur, V. K. (2011). Crustal structure of the Darjeeling-Sikkim Himalaya and southern Tibet. *Geophysical Journal International*, *184*(2). https://doi.org/10.1111/j.1365-246X.2010.04868.x

Adlakha, V., Lang, K. A., Patel, R. C., Lal, N., & Huntington, K. W. (2013). Rapid long-term erosion in the rain shadow of the Shillong Plateau, Eastern Himalaya. *Tectonophysics*, *582*, 76-508 83

Aoya, M., Wallis, S. R., Kawakami, T., Lee, J., Wang, Y., & Maeda, H. (2006). The Malashan gneiss dome in south Tibet: Comparative study with the Kangmar dome with special reference to kinematics of deformation and origin of associated granites.

Aoya, M., Wallis, S. R., Terada, K., Lee, J., Kawakami, T., Wang, Y., & Heizler, M. (2005). North-south extension in the Tibetan crust triggered by granite emplacement. *Geology*, *33*(11), 853-856.

Avouac, J. P. (2003). Mountain building, erosion, and the seismic cycle in the Nepal Himalaya. *Advances in geophysics*, *46*, 1-80.

Braun, J. (2003). Pecube: A new finite-element code to solve the 3D heat transport equation including the effects of a time-varying, finite amplitude surface topography. *Computers and Geosciences*, *29*(6), 787–794. https://doi.org/10.1016/S0098-3004(03)00052-9

Braun, J., & Robert, X. (2005). Constraints on the rate of post-orogenic erosional decay from low-temperature thermochronological data: Application to the Dabie Shan, China. *Earth Surface Processes and Landforms: The Journal of the British Geomorphological Research Group*, *30*(9), 1203-1225.

Braun, J., van der Beek, P., Valla, P., Robert, X., Herman, F., Glotzbach, C., Pedersen, V., Perry, C., Simon-Labric, T., & Prigent, C. (2012). Quantifying rates of landscape evolution and tectonic processes by thermochronology and numerical modeling of crustal heat transport using PECUBE. In *Tectonophysics* (Vols. 524–525, pp. 1–28). https://doi.org/10.1016/j.tecto.2011.12.035

Clubb, F. J., Mudd, S. M., Schildgen, T. F., van der Beek, P. A., Devrani, R., & Sinclair, H. D. (2023). Himalayan valley-floor widths controlled by tectonically driven exhumation. *Nature Geoscience*, *16*(8), 739-746.

Coutand, I., Whipp, D. M., Grujic, D., Bernet, M., Fellin, M. G., Bookhagen, B., Landry, K. R., Ghalley, S. K., & Duncan, C. (2014). Geometry and kinematics of the Main Himalayan Thrust and Neogene crustal exhumation in the Bhutanese Himalaya derived from inversion of multithermochronologic data. *Journal of Geophysical Research: Solid Earth*, *119*(2). https://doi.org/10.1002/2013JB010891

DeCelles, P. G., Gehrels, G. E., Najman, Y., Martin, A. J., Carter, A., & Garzanti, E. (2004). Detrital geochronology and geochemistry of Cretaceous–Early Miocene strata of Nepal: implications for timing and diachroneity of initial Himalayan orogenesis. *Earth and Planetary Science Letters*, *227*(3-4), 313-330.

Deeken, A., Thiede, R. C., Sobel, E. R., Hourigan, J. K., & Strecker, M. R. (2011). Exhumational variability within the Himalaya of northwest India. *Earth and Planetary Science Letters*, *305*(1–2), 103–114. https://doi.org/10.1016/j.epsl.2011.02.045

Dèzes, P. (1999). *Tectonic and metamorphic evolution of the central Himalayan domain in south-east Zanskar (Kashmir, India)* (Doctoral dissertation, Université de Lausanne, Faculté des sciences).

Ge, Y., Liu-Zeng, J., Zhang, J., Wang, W., Tian, Y., Fox, M., ... & Xie, K. (2020). Spatio-temporal variation in rock exhumation linked to large-scale shear zones in the southeastern Tibetan Plateau. *Science China Earth Sciences*, *63*(4), 512-532.

Grujic, D., Warren, C. J., & Wooden, J. L. (2011). Rapid synconvergent exhumation of Miocene-aged lower orogenic crust in the eastern Himalaya. *Lithosphere*, *3*(5). https://doi.org/10.1130/L154.1

Hack, J. T. (1957). Studies of longitudinal stream profiles in Virginia and Maryland (Vol. 294). US Government Printing Office.

Hazarika, D., Wadhawan, M., Paul, A., Kumar, N., & Borah, K. (2017). Geometry of the Main Himalayan Thrust and Moho beneath Satluj valley, northwest Himalaya: Constraints from receiver function analysis. *Journal of Geophysical Research: Solid Earth*, *122*(4). https://doi.org/10.1002/2016JB013783.

Herman, F., Copeland, P., Avouac, J. P., Bollinger, L., Mahéo, G., Le Fort, P., Rai, S., Foster, D., Pêcher, A., Stüwe, K. & Henry, P. (2010). Exhumation, crustal deformation, and thermal structure of the Nepal Himalaya derived from the inversion of thermochronological an the-mobarometric data and modeling of the topography. *Journal of Geophysical Research: Solid Earth*, *115*(B6)

Hofmann-Wellenhof, B., & Moritz, H. (2006). Physical Geodesy (2nd, corr. ed. 2006 edition ed.). Wien ; New York: Springer.

Horton, F., Lee, J., Hacker, B., Bowman-Kamaha'o, M., & Cosca, M. (2015). Himalayan gneiss dome formation in the middle crust and exhumation by normal faulting: New geochronology of Gianbul dome, northwestern India. *Bulletin*, *127*(1-2), 162-180.

Kirby, E., & Whipple, K. X. (2012). Expression of active tectonics in erosional landscapes. Journal of Structural Geology, 44, 54–75. https://doi.org/10.1016/j.jsg.2012.07.009.

Kumar, A., Lal, N., Jain, A. K., & Sorkhabi, R. B. (1995). Late cenozoic-quaternary thermo-tectonic history of Wigher Himalayan Crystalline (HHC) in Kishtwar-Padar-Zanskar region, NW Himalaya: Evidence from fission track ages. *Journal Geological Society of India*, *45*(4), 375-391.

Larson, K. P., Godin, L., Davis, W. J., & Davis, D. W. (2010). Out-of-sequence deformation and expansion of the Himalayan orogenic wedge: Insight from the Changgo culmination, south central Tibet. *Tectonics*, *29*(4).

Lee, J., Hacker, B. R., Dinklage, W. S., Wang, Y., Gans, P., Calvert, A., ... & McClelland, W. (2000). Evolution of the Kangmar Dome, southern Tibet: Structural, petrologic, and thermochronologic constraints. *Tectonics*, *19*(5), 872-895.

Lee, J., McClelland, W., Wang, Y., Blythe, A., & McWilliams, M. (2006). Oligocene–Miocene middle crustal flow in southern Tibet: Geochronology of Mabja Dome.

Ma, Z., Han, Z., Li, Y., Xu, T., Han, X., Bi, W., & Zhang, W. (2023). Late Cenozoic cooling and evolution history of the Kangmar dome in southern Tibet: Insights from inverse thermal modeling. *Frontiers in Earth Science*, *11*, 1186901.

Mitra, S., Priestley, K., Bhattacharyya, A. K., & Gaur, V. K. (2005). Crustal structure and earthquake focal depths beneath northeastern India and southern Tibet. *Geophysical Journal International*, *160*(1). https://doi.org/10.1111/j.1365-246X.2004.02470.x

Mudd, S. M., Clubb, F. J., Gailleton, B., & Hurst, M. D. (2018). How concave are river channels? Earth Surface Dynamics, 6(2), 505–523. https://doi.org/10.5194/esurf-6-505-2018.

Mudd, Simon M., et al. "A statistical framework to quantify spatial variation in channel gradients using the integral method of channel profile analysis." *Journal of Geophysical Research: Earth Surface* 119.2 (2014): 138-152.

Naito, N., Ageta, Y., Iwata, S., Matsuda, Y., Suzuki, R., & Yabuki, H. (2006). Glacier shrinkages and climate conditions around Jichu Dramo Glacier in the Bhutan Himalayas from 1998 to 2003. *Bulletin of glaciological research*, *23*, 51-61.

NASA Shuttle Radar Topography Mission (SRTM)(2013). Shuttle Radar Topography Mission (SRTM) Global. Distributed by OpenTopography. https://doi.org/10.5069/G9445JDF.

Oliveira Jr, V. C., Uieda, L., Hallam, K. A., & CF, V. (2018). Should geophysicists use the gravity disturbance or the anomaly?. *Geophysics*.

Pérez-Peña, J. V., Al-Awabdeh, M. O. H. A. M. M. A. D., Azañón, J. M., Galve, J. P., Booth-Rea, G., & Notti, D. (2017). SwathProfiler and NProfiler: Two new ArcGIS Add-ins for the automatic extraction of swath and normalized river profiles. *Computers & Geosciences*, *104*, 135-150.

Quigley, M., Liangjun, Y., Xiaohan, L., Wilson, C. J., Sandiford, M., & Phillips, D. (2006). 40Ar/39Ar thermochronology of the Kampa Dome, southern Tibet: Implications for tectonic evolution of the North Himalayan gneiss domes. *Tectonophysics*, *421*(3-4), 269-297.

Sambridge, M. (1999a). Geophysical inversion with a neighbourhood algorithm - I. Searching a parameter space. *Geophysical Journal International*, *138*(2). https://doi.org/10.1046/j.1365-246X.1999.00876.x.

Sambridge, M. (1999b). Geophysical inversion with a neighbourhood algorithm--II. Appraising the ensemble. *Geophysical Journal International*, *138*(3). https://doi.org/10.1046/j.1365-246X.1999.00900.x.

Shen, T., Wang, G., Leloup, P. H., van Der Beek, P., Bernet, M., Cao, K., ... & Zhang, K. (2016). Controls on Cenozoic exhumation of the Tethyan Himalaya from fission-track thermochronology and detrital zircon U-Pb geochronology in the Gyirong basin area, southern Tibet. *Tectonics*, *35*(7), 1713-1734.

Sorkhabi, R. B., Jain, A. K., Itaya, T., Fukui, S., Lal, N., & Kumar, A. (1997). Cooling age record of domal uplift in the core of the Higher Himalayan Crystallines (HHC), southwest Zanskar, India. *Journal of Earth System Science*, *106*(3), 169-179.

Thiede, R., Robert, X., Stübner, K., Dey, S., & Faruhn, J. (2017). Sustained out-of-sequence shortening along a tectonically active segment of the Main Boundary thrust: The Dhauladhar Range in the northwestern Himalaya. *Lithosphere*, *9*(5), 715-725.

Valla, P. G., Herman, F., van Der Beek, P. A., & Braun, J. (2010). Inversion of thermochronological age-elevation profiles to extract independent estimates of denudation and relief history—I: Theory and conceptual model. *Earth and Planetary Science Letters*, *295*(3-4), 511-522.

Warren, C. J., Grujic, D., Kellett, D. A., Cottle, J., Jamieson, R. A., & Ghalley, K. S. (2011). Probing the depths of the India-Asia collision: U-Th-Pb monazite chronology of granulites from NW Bhutan. *Tectonics*, *30*(2). https://doi.org/10.1029/2010TC002738.

Yadav, D. K., Hazarika, D., & Kumar, N. (2016). Seismicity and stress inversion study in the Kangra–Chamba region of north-west Himalaya. *Natural Hazards*, *82*(2), 1393–1409. https://doi.org/10.1007/s11069-016-2251-y.

Zhao, W., Nelson, K. D., Che, J., Quo, J., Lu, D., Wu, C., & Liu, X. (1993). Deep seismic reflection evidence for continental underthrusting beneath southern Tibet. *Nature*, *366*(6455). https://doi.org/10.1038/366557a0.